Zircon Xenocrysts from Cenozoic Alkaline Basalts of the Ratanakiri Volcanic Province (Cambodia), Southeast Asia—Trace Element Geochemistry, O-Hf Isotopic Composition, U-Pb and (U-Th)/He Geochronology—Revelations into the Underlying Lithospheric Mantle

Paula C. Piilonen [1],*, F. Lin Sutherland [2] , Martin Danišík [3], Glenn Poirier [1], John W. Valley [4] and Ralph Rowe [1]

[1] Mineralogy Section, Beaty Centre for Species Discovery, Research & Collections, Canadian Museum of Nature, P.O. Box 3443, Station D, Ottawa, Ontario K1P 6P4, Canada; gpoirier@nature.ca (G.P.); rrowe@nature.ca (R.R.)

[2] Geoscience, Australian Museum, 1 William Street, Sydney NSW 2010, Australia; linsutherland1@gmail.com

[3] John de Laeter Centre, The Institute for Geoscience Research (TIGeR), Curtin University, Perth WA 6845, Australia; m.danisik@curtin.edu.au

[4] Wisconsin Secondary Ion Mass Spectrometer Laboratory (WiscSIMS), Department of Geoscience, University of Wisconsin, Madison, Wisconsin 53706, USA; valley@geology.wisc.edu

* Correspondence: ppiilonen@nature.ca

Abstract: Zircon xenocrysts from alkali basalts in Ratanakiri Province, Cambodia represent a unique low-Hf zircon within a 12,000 km long Indo-Pacific megacryst zone. Colorless, yellow, brown, and red crystals ({100}, {101}, subordinate {211}, {1103}), with hopper growth and corrosion features range up to 20 cm in size. Zircon chemistry indicates juvenile, Zr-saturated, mantle-derived alkaline melt (Hf 0.6–0.7 wt %, Y <0.2 wt %, U + Th + REE (Rare-Earth Elements) < 600 ppm, Zr/Hf 66–92, Eu/Eu*$_N$ ~1, positive Ce/Ce*$_N$, HREE (Heavy REE) enrichment). Incompatible element depletion with increasing Yb/Sm$_N$ from core to rim at ~ constant Hf suggests single stage growth. Ti-in-zircon temperatures (~570–740 °C) are lower than predicted by crystal morphology (800–900 °C) and decrease from core to rim (ΔT = 10–50 °C). The $\delta^{18}O$ values (4.88 to 5.01‰ VSMOW (Vienna Standard Mean Ocean Water)) are relatively low for xenocrysts from the zircon Indo-Pacific zone (ZIP). The $^{176}Hf/^{177}Hf$ values (+ εHf 4.5–10.2) give T$_{Depleted\ Mantle}$ model source ages of 260–462 Ma and T$_{Crustal}$ ages of 391–754 ma. The source magmas reflect variably depleted lithospheric mantle with little supracrustal input. Zircon U-Pb (0.88–1.56 Ma) and (U-Th)/He (0.86–1.02 Ma) ages are older than host basalt ages (~0.7 Ma), which suggests limited residence before transport. Zircon genesis suggests Zr-saturated, Al-undersaturated, carbonatitic-influenced, low-degree partial melting (<1%) of peridotitic mantle at ~60 km beneath the Indochina terrane.

Keywords: zircon; xenocryst; alkali basalt; Ratanakiri Volcanic Province; trace elements; O-isotopes and Hf-isotopes; U-Pb; (U-Th)/He

1. Introduction

Southeast (SE) Asia is an important source of gem corundum and zircon [1–3]. Recent and paleo-alluvial gem deposits occur in Thailand, Cambodia, Vietnam, and Laos, as deposits in a belt

that extends >12,000 km along the west Pacific continental margins south to Australia and north to eastern China and Russia. This belt is known as the zircon megacryst (xenocryst) Indo-Pacific zone (ZIP, Figure 1) [4–14]. The western Pacific margin is marked by dynamic tectonic settings in which plate motions carry both continental and former sea-floor lithosphere over zones of hot upwelling asthenosphere. All SE Asian deposits are associated with late Cenozoic (<30 Ma) intraplate alkaline basaltic volcanism, which is the result of onset of decompression melting and an extensional tectonic regime in SE Asia following the Himalayan orogeny [15,16]. In SE Asia, intraplate alkali basalt magmas erupted through the late Precambrian to early Cenozoic along roughly northward-trending rifted blocks and fold belt terranes flanking the Indochina cratonic block.
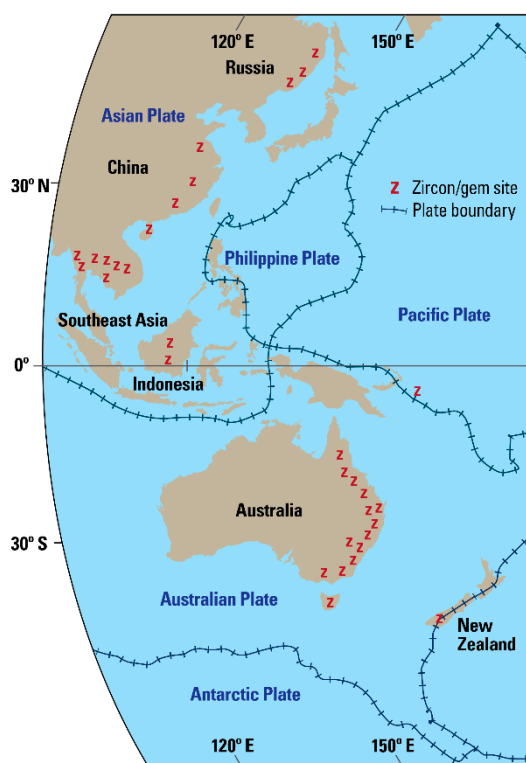

Figure 1. Map showing the 12,000 km long zircon megacryst Indo-Pacific zone (ZIP) along the western Pacific continental margins in Eastern Australasia, Asia, and Russia. The intraplate basalts hosting the megacryst suites are dominantly alkaline in composition and involve deeper mantle generation of magmas that may intersect pre-existing gem-bearing felsic or metamorphic bodies [11]. Consult this reference for zircon locality details.

Gem zircon and corundum xenocrysts, which have been eroded out of the host alkali basalts during the production of lateritic soils are concentrated into economic-grade deposits by secondary processes [17]. Mining for xenocrystic gems has taken place since the early 1400s in Thailand (Chanthaburi-Trat) and the late 1880s in Cambodia (Pailin and Ratanakiri provinces). In some deposits, zircon dominates over corundum, as is the case within the Ratanakiri Volcanic Province (RVP). Mechanized mining continues today in parts of Thailand but in Cambodia, small-scale artisanal mining by Vietnamese, Burmese and local indigenous peoples is common, often utilizing the same primitive techniques used hundreds of years ago.

Zircon is a ubiquitous accessory mineral in a wide range of rock types including mafic and felsic rocks derived from both crustal and mantle sources, lunar rocks, tektites, and metamorphic rocks [18]. It is chemically resistant and can survive weathering and transport processes, which allow it to be concentrated in secondary placer heavy mineral deposits. Zircon is highly refractory and has a low solubility in most melt and fluid compositions, which allows it to survive almost any crustal process

including high temperature metamorphism and anatexis. Although the abundance of zircon is low, it has a strong effect on the behavior of many trace elements during crystallization and, thus, is an important accessory mineral in understanding petrogenesis. Furthermore, the low diffusion rates of rare-earth elements (REE), Th, U, Pb, Hf, and O in zircon under most geological conditions conserves both trace element composition zoning and the isotopic signature, which offers a window into its growth, evolution, and recycling events.

Xenocrystic zircon are known from many Cenozoic alkaline basalt provinces world-wide. However, their origins, petrogenesis, and relationship with their host basaltic rocks are still widely debated. Most authors are in agreement with a mantle source for some xenocrystic suites. However, the exact geochemical, isotopic, and mineralogical characteristics of this source are not completely known. Boehnke et al. [19] performed experimental studies on Zr saturation in mafic (basaltic) melts and concluded that such melt compositions require an unrealistically high concentration of Zr (>5000 ppm) to directly crystallize zircon. As such, zircon within ZIP basalts must have crystallized from late-stage, evolved magmas and become entrained in the rising alkali basalt host. Additional experimental studies on Zr saturation in alkaline melts, silicate, or carbonatitic are limited and focused on intermediate to felsic crustal compositions (e.g., [20–22]). More information is needed concerning Zr saturation under upper mantle conditions before inferences can be made about the petrogenesis of zircon xenocrysts. By utilizing trace element geochemistry, isotopic systems that reflect original magmatic conditions (i.e., O and Hf) and comparisons of the crystallization and eruption ages of the xenocrysts within the host basalts. Insights can be gained on the origin of these zircons.

This study presents field and laboratory studies started in 2012 investigating the zircon megacrysts which are being mined from the RVP basaltic gem fields in Northeastern Cambodia.

A recent study on similar zircons [23] has provided valuable new data on one set of RVP zircon megacrysts. However, the present study differs in reporting on a wider range of zircon samples and their color and form variants from several well-defined localities as well as providing further analytical and literature results. Some detailed comparisons of the two data sets are incorporated, which allows for wider discussion and interpretations on the origin of these Cambodian zircons. This study is the first of its kind in Cambodia and provides insight into understanding the composition and the evolutionary history of the subcontinental lithospheric mantle (SCLM) in Northeast Cambodia.

2. General Geology

Southeast Asia including Thailand and Cambodia is an assemblage of distinct terranes amalgamated together to form two dominant crustal blocks known as the Indochina and the Shan-Thai (or Sibumasu) terranes (Figure 2). These two terranes are separated and overprinted by Mesozoic and younger arc systems of the Sukhothai Zone (Fold Belt) and the Sa Kaeo Suture Zone (SKS). Although these two terrains have separate geological histories, they both have their origins at the margin of Gondwana prior to collision during the Mesozoic [24]. The Indochina terrain, which extends from Eastern Thailand, Laos, across Cambodia, and into Southern Vietnam, rifted away from the northern edge of Gondwanaland during the Devonian. This resulted in the opening of Paleotethys [25]. Little is known about the Precambrian tectonic history of Thailand and Cambodia even though gneisses and schists of the Proterozoic Kontum massif in Vietnam extend into Northeast Cambodia near the border with Thailand [26]. Similar high-grade metamorphic rocks have been found in Pailin along the border with Thailand [26,27].

Collision and convergence of the Indochina block with the Asian continent (Shan-Thai terrane in Thailand) started at ~250 Ma and culminated around the Triassic-Jurassic boundary (~210–200 Ma) with the closure of Paleotethys and the end of the Indosinian orogeny [25,26]. The Indochina terrain is composed of continental crust, which has remained intact and stable since the end of the Indosinian orogeny, and is surrounded by younger, post-Jurassic fold belts. Cambodia lies entirely in the Indochina terrain between the Truongson fold belt to the north and the Loei fold belt to the west. Both of these regions contain Carboniferous to Triassic collisional arc-type volcanosedimentary sequences.
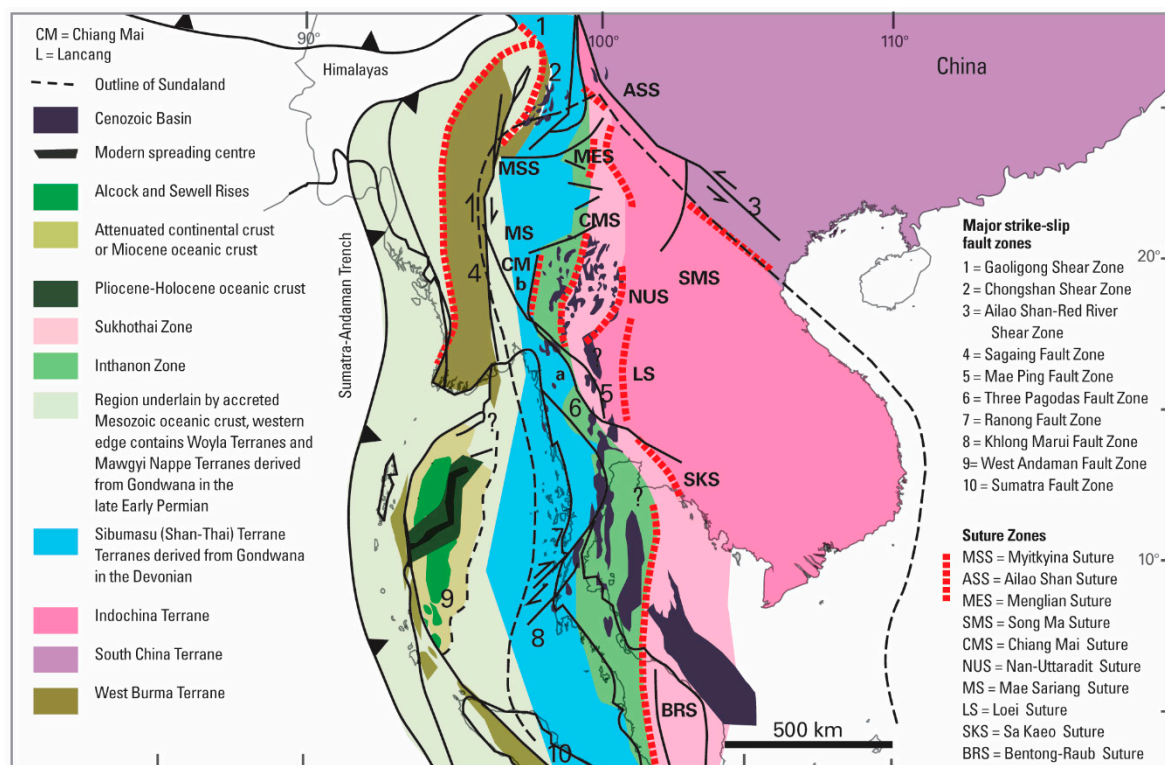
Figure 2. Tectonic map of SE Asia [25]. Cambodia is entirely contained within the Indochina terrain bounded on the northeast by the Song Ma Suture (SMS).

The Cenozoic tectonic evolution of Cambodia and Thailand is related to the collision between the Indian and Eurasian plates during the Himalayan Orogeny (55–45 Ma, [28]). Compressional stresses dominating in the northern part of the collisional zone resulted in the Southeast China block and adjacent parts of Southeast Asia (Indosinia) to be rotated and forced to the southeast [29], which results in uplift and transtension and graben structures with predominantly a NW-SE strike along with the opening of the Gulf of Thailand, the South China Sea, and the Andaman Sea [30]. Uplift, extensional tectonics and rifting throughout SE Asia resulted in lithospheric thinning, which triggered decompressional melting and upwelling of the underlying asthenosphere along deep-seated faults to form late Cenozoic flood basalts [16,29]. ZIP fields across SE Asia are flanked to the east by extinct marginal spreading basins and offset rifts that formed behind the Pacific island arc-subduction system [31]. These basins involved thermal rifting and could provide a continuous source of sub-lithospheric melting to promote zircon (and corundum) crystallization during prolonged basaltic events [11,32,33].

Cenozoic basalts occur throughout SE Asia (red regions, Figure 3) ranging in age from 24 Ma to as recently as a 1923 eruption off the Vietnamese coast near the island of Poulo Cécir [34,35]. Known collectively as the SE Asian Volcanic Province [36–38] or the Central-East Asian basaltic province [8], the basalts ascended along rift structures bounded by strike-slip faults within Archean to Paleozoic terrains and were more extensive in Vietnam, Eastern Cambodia, and Southern Laos than elsewhere in the region even though no temporal and spatial correlation has been established [39]. In most areas, two separate periods of volcanism are noted: (1) an early phase consisting of SiO_2-rich, Fe-depleted, and Ti-depleted quartz and olivine tholeiites and rare trachyandesites, representative of lithospheric sources, and (2) a later, highly alkaline phase consisting of lower SiO_2, high Fe, and Ti olivine tholeiites, alkali basalts, basanites, and rare trachybasalts and trachytes, representative of asthenospheric mantle sources [16,40]. Zircon and corundum xenocrysts are associated with late-stage, alkaline phases of volcanism [16,29,41].

Figure 3. Distribution of Cenozoic alkali basalt provinces (red) in SE Asia (modified after [16]). The location of the Ratanakiri Volcanic Province (RVP) is shown as a red circle.

2.1. Ratanakiri Volcanic Province (RVP)

Detailed geological information about Cambodia is difficult to obtain as a result of the destruction of all academic material by the Khmer Rouge. Early work by Lacombe [42,43] concerning the geology, geochemistry, and mineralogy of the RVP basalts is still the most definitive work in existence. Previous 1:500,000 maps by both France (1970s) and Russia (1990) are out of date. Little work has been completed in the country since that time. Detailed mapping, age dating, and geochemical analyses of the rocks in the RVP is currently underway by the lead author.

Quaternary basaltic rocks cover approximately 10,000 km^2 of the country and overlie Quaternary alluvium and Mesozoic sediments. Small flows and vents occur in the west near Pailin and Poipet and in the central northern province of Preah Vihear. Two distinctly larger basaltic areas are found in Ratanakiri province (Figure 4) and comprise the fifth largest basaltic plateau in Indochina: (1) the Bokeo plateau is located between the Sre Pok and the Sesan rivers, herein referred to as the Ratanakiri Volcanic Province (RVP), and it is host to xenocrystic gem zircon deposits and (2) the smaller, zircon-free Ban Chay plateau, northeast of Bokeo and north of the Sesan river near the Vietnamese border [42]. Lacombe [42] estimated the thickness of the basalt plateaus to 80 m near the center and 40 m closer to the extremities. Initially the flows would have covered an area of around 3200 km^2, but now weathered down to under 2000 km^2 (RVP: 1500 km^2, Ban Chay Plateau: 200 km^2). The initial topographic relief was quickly filled by the early flows, which allows later flows to spread in all directions and cover a wide area with thin, individual flows (often <2 m thick). Lacombe [42] observed only alkaline basalts in the Ban Lung area (olivine basalts, alkali basalts, basanites, nephelinites, and trachyandesites). He also noted that early flows preceded the last paleomagnetic inversion (0.7 Ma) and the later, more explosive basaltic volcanism occurred during and after the geomagnetic reversal. This falls within the range (17.6–0 Ma) established by Hoang & Flower [40] for related basaltic volcanism in Vietnam and other Cenozoic volcanism throughout the Northwestern Pacific continental margin.
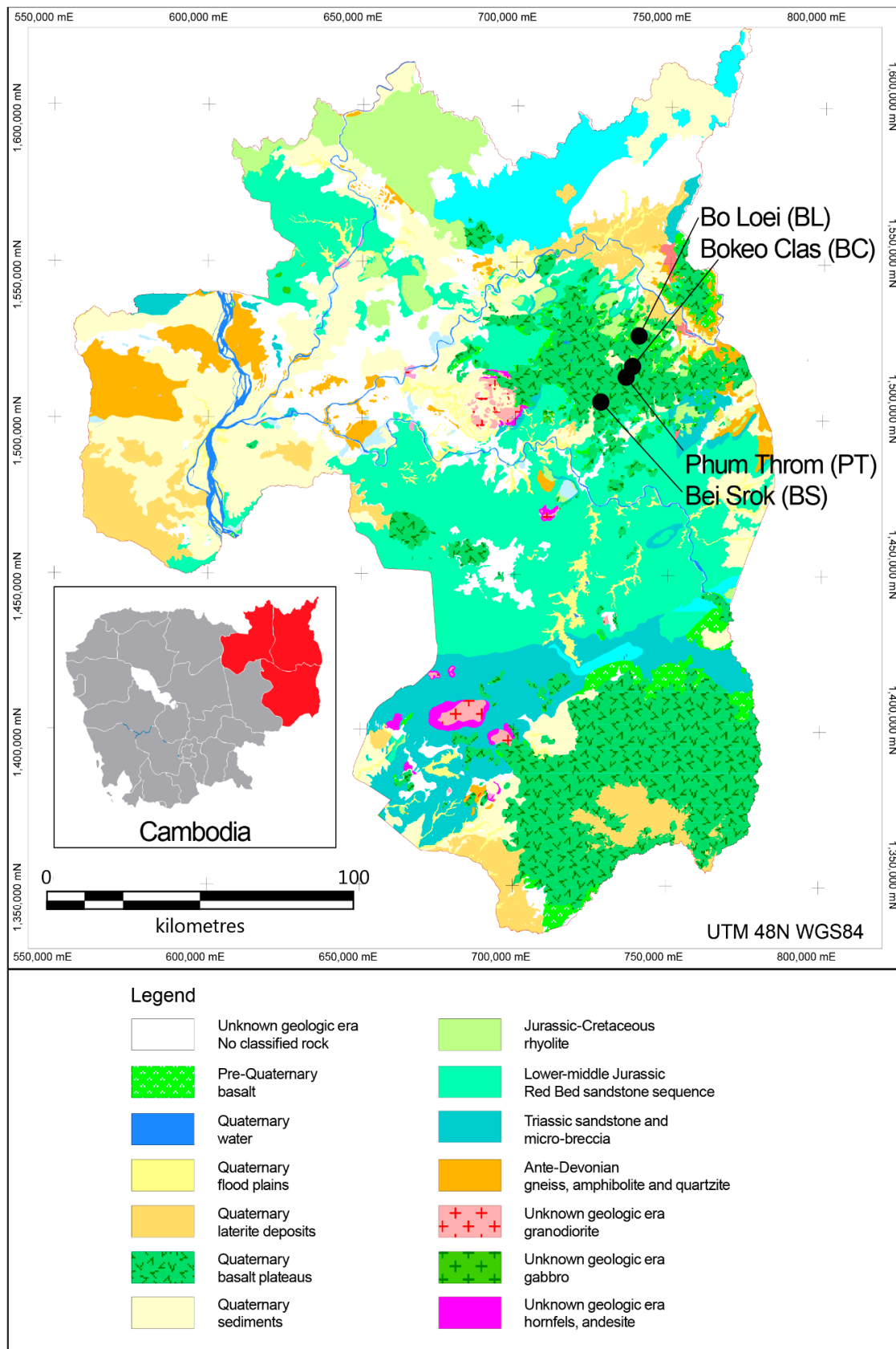
Figure 4. Geological map of Stung Treng, Ratanakiri, and Mondulkiri provinces, Northeast Cambodia. The Ratanakiri Volcanic Province (RVP) and Ban Chay Plateau Quaternary basalts are indicated in green with hatching. Zircon xenocryst localities (black dots) include Bokeo Clas (BC), Phum Throm (PT), Bei Srok (BS), and Bo Loei (BL).

Basaltic volcanism began with fissure flows. A brief, erosional hiatus was followed by increasingly more explosive volcanism from both old and new fissures [42]. The final stage was even more explosive and resulted in craters and deposits of mafic scoria, ignimbrite, welded tuff, tuff, ash flows, and pumice. Volcanic features include: (1) scoria cones (1–3 km wide × 150 m tall), (2) horseshoe craters, which have been opened as a result of extensive erosion, (3) crater cones, (4) explosive craters, and (5) rift valleys and volcanotectonic depressions [42,44]. Many of these structures are only recognizable from air photos and satellite imagery since complete volcanic profiles in the RVP have extensive lateritization and vegetative cover.

2.2. Zircon Deposits

In situ zircon is extremely rare and has only been collected by the senior author in alkali basalt at Phnom Dang, Bokeo (Figure 5), which is an alkali basalt scoria outcrop on the flank of the Phnom Dang scoria cone, and from a tephriphonolite flow 3 km SE of Phnom Dang, Bokeo. Lacombe [43] also noted the presence of xenocrysts in trachybasalt/alkali basalts and associated pyroclastics at Phnom Dang, Bo Tum and Bo Loei. At all localities, zircon occurs as single crystals in the alkali basalt without other xenocrystic minerals. Gem zircon, which is derived from the alkali basalts, is mined from secondary deposits within a roughly NE–SW trending region ~30 km in strike, 10 km wide, east of the provincial capital of Ban Lung (Figure 4). Unlike deposits in other west Pacific continental margin regions including Western Cambodia and Southeastern Thailand and gem deposits in the RVP contain dominantly zircon with only trace corundum. Zircon mines in Ratanakiri are small-scale affairs-gem-quality stones are found in the residual soils and gravels derived from weathered basalts. The gemstones are mined by digging vertical pits (10 m deep, 1 m wide) to bedrock and hauling to surface the lateritic soils and basalt gravels in which loose xenocrysts are concentrated. On the surface, other miners sift through the soil with their hands to extract the zircons. In rare cases, during the wet season, pressured water is used to loosen the lateritic soil and wash out the zircons. Only 20% of zircon are actually valuable as gem stones. Many of the stones are fractured, contain inclusions, or are an unsuitable color. Zircon from Bei Srok (BS) has historically been the most sought after by the gem industry due to its dark red color, which, when heat-treated in a reduced environment, changes to a dark, more brilliant blue color (Figure 5). An electron-related or hole-related color center is thought to be the cause of dark red-brown color in the RVP zircon while authors have not yet been able to unequivocally determine the mechanism for the blue coloration upon heat-treating [45]. The highest quality gem zircon is found at the Bei Srok deposit, which is 16 km south of the provincial capital of Ban Lung at the southern end of the gem-bearing region. The Bokeo Clas (BC) and Phum Throm (PT) deposits are located 23 km east of Ban Lung near the village of Bokeo and represent the most prolific mining areas. Other less significant occurrences are known throughout the Bokeo plateau where locals pan for zircon in the creeks and riverbeds. Rare blue-green corundum has been found in zircon concentrates from Bei Srok.

The Bo Loei (BL) deposit is located 24 km ENE of Ban Lung, 28 km W from the Vietnamese border, and 28 km NNE of Bei Srok. BoLoei marks the northern-most gem occurrence and comprises an alluvial wash containing xenocrysts of zircon, corundum (blue, blue-green, and yellow-orange), and spinel as well as fragments of alkali basalt, felsic volcanics (rhyolite), and other country rock. Bo Loei is principally a gem zircon deposit with corundum as a by-product (<3% of the total yield, [12]). The water table at Bo Loei is higher than that at other Ratanakiri zircon deposits, which allows for panning and concentration of the zircon ore in nearby streams.

(**a**)	(**b**)

Figure 5. (**a**) Zircon miner at Phum Throm, Ratanakiri, Cambodia. (**b**) Natural and heat-treated faceted RVP zircon (each stone is ~0.75 carats). Photo copyright M. Bainbridge, Canadian Museum of Nature collection.

3. Materials and Methods

3.1. Sample Descriptions

Zircon crystals from the RVP range in size from $2 \times 2 \times 4$ mm to $15 \times 20 \times 20$ cm long (average: $7 \times 8 \times 8$ mm). Crystals are subhedral to euhedral, dominantly vitreous to adamantine, transparent grey-yellow, honey yellow, pinkish-orange, light orange-brown, and dark red with minor translucent to opaque milky-grey and yellow crystals. Squat prismatic crystals dominated by {100} and {101} are most typically euhedral. Less common crystal forms include the {211} bipyramid and {110} prism and more often occur in subhedral grains. Prismatic zircon ranges in color from transparent light yellow to dark red to highly-included, translucent milky-yellow and red-brown. Subhedral to anhedral multiform zircon are most often transparent and range in color from light orange-yellow to orange-red to dark red. Sharp, concentric color zoning is evident optically in many crystals, which corresponds to zoning observed in back-scattered electron (BSE) and cathodoluminescence (CL) images. In situ zircon occurs solely as isolated grains within the alkali basalt (Figure 6a,b). The interface between the zircon and the host alkali basalt is characterized by a very thin (1–2 µm) glassy reaction rim with numerous fine fractures, which is indicative of contraction of the glass upon cooling. The presence of such a discrete, quenched glassy interface without evidence for chemical interaction suggests a wide temperature difference between the entrained zircon and the host basaltic magma.

The majority of Ratanakiri zircon display striking resorption and corrosion features along with hopper-type growth patterns (Figure 6c) indicative of disequilibrium with their host magmas. Subhedral to euhedral zircon are often dominated by a short prism capped by a bipyramid on one termination and a hopper-type growth feature on the bottom termination. This hopper-type or corroded habit appears to represent an attachment point with an associated xenocrystic phase on the growth medium. However, multimineralic xenoliths containing zircon have not been found to confirm these possible intergrowths. Late-stage dendritic etching in-filled by baddeleyite is also present on many crystals (Figure 6d), which indicates late-stage interaction with a highly-alkaline corrosive melt or fluid, and remobilization of Zr. Fluid inclusions dominated by H_2O with rare CO_2 bubbles were found by Zeug et al. [45] in a number of RVP zircon xenocrysts. Partially healed fissures surrounded many of the fluid inclusions.

Zircon from Bo Loei is commonly subhedral to anhedral and does not display the etching, dissolution, and corrosion features that are common to other Ratanakiri zircon, which is possibly a result of increased transport in alluvial or fluvial systems.
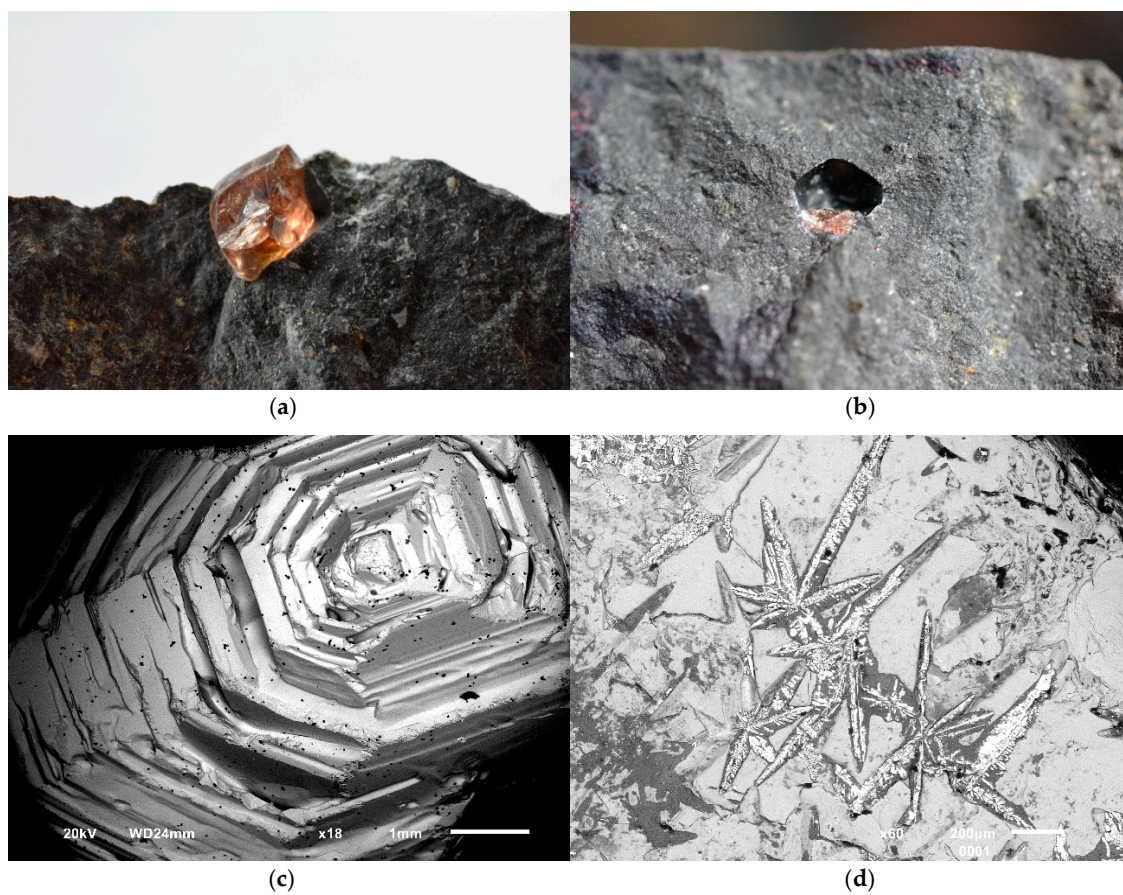
Figure 6. Zircon xenocrysts from the RVP: (**a**) euhedral zircon (7 × 4.5 × 4 mm) in situ from Phnom Dang, Bokeo. (**b**) Glassy reaction rim (1–2 µm wide lining the 5 mm hole) between zircon xenocryst and the host alkali basalt. (**c**) Hopper-type growth feature on the subhedral zircon. (**d**) Late-stage dendritic etching in-filled by baddeleyite on the surface of a zircon xenocryst.

All zircon samples were purchased directly from miners at each locality. Representative zircon grains ranging in size from 4 × 4 × 4 mm to 19 × 11 × 8 mm were hand-picked under a binocular microscope and mounted in epoxy blocks for analysis. The blocks were cut in half, laterally, on a thin section saw to expose the interior center of the grains prior to being polished.

3.2. Cathodoluminescence Microscopy and Electron Microprobe Analyses

Cathodoluminescence (CL) and back-scattered electron imaging (BSEI) was done on a JEOL 6610Lv scanning electron microscope (JEOL USA Inc., Peabody, MA, USA) operating at 20 kV with a spot size of 55 µm and a working distance of 20 mm. The SEM was equipped with a monochromatic Gatan miniCL detector (Gatan Inc., Pleasanton, CA, USA). Chemical analyses of the zircon xenocrysts were done with a JEOL Superprobe 8230 (JEOL USA Inc., Peabody, MA, USA) at the University of Ottawa. Operating conditions were as follows: beam diameter of 5 µm, operating voltage 20 kV, and a beam current of 40 nA. A total of six elements were sought and the following standards and *X*-ray lines were employed: synthetic YIG garnet (Y $L\alpha$), zircon (Zr $L\alpha$, Si $K\alpha$), synthetic UO_2 (U $M\alpha$), synthetic ThO_2 (Th $M\alpha$), and hafnon (Hf $M\alpha$). Count times for Zr, Th, U, and Si were 20 s on peak and 10 s on the background and count times on Hf and Y were 50 s on peak and 25 s on the background. Raw intensities were corrected by using the PAP routine [46]. The Hf concentrations obtained by EMPA (Table 1) were used as an internal standard for trace element determination by laser ablation inductively-coupled plasma mass spectrometry (LA-ICP-MS).

3.3. Trace-Element Analysis

Trace element contents were analyzed by using an Agilent 7700 quadrupole ICP-MS instrument (Agilent Technologies, Santa Clara, CA, USA) attached to a Photon Machines Excimer 193 nm laser system (Excite, Photon machines Inc., Redmond, WA, USA) at the Macquarie University. The analyses were carried out by using the same laser conditions as for U-Pb dating. Detailed descriptions of analytical and calibration procedures have been given by Belousova et al. [5]. Quantitative results for 25 elements reported in this paper were obtained through calibration of relative element sensitivities using the NIST-610 standard glass and the GEMOC GJ-1 and Mud Tank zircon standards [47] as the external calibration standard as well as normalization of each analysis to the EMPA data for Hf as an internal standard. The precision and accuracy of the NIST-610 analyses are 1–2% for REE, Y, Sr, Nb, Hf, Ta, Th, and U at the ppm concentration level, 4% for Ti, 5% for Pb, and 20% for P at ppm concentrations.

3.4. Hf-Isotope Analysis

Methodology and an analytical condition for the Lu-Hf isotope analysis are provided by Griffin et al. [48]. Hf-isotope analyses were carried out in situ using a New Wave/Merchantek UP-213 laser-ablation microprobe (New Wave Research, Inc., Petach Tikva, Israel), attached to a Nu Plasma multi-collector ICP-MS (Nu Instruments Ltd., Wrexham, UK) at Macquarie University. The analyses were carried out with a beam diameter 55 μm and a 5 Hz repetition rate. Typical ablation times were 100–120 s and resulted in pits 30–40 μm deep. The ablated sample was transported by He carrier gas from the laser-ablation cell via a mixing chamber to the ICP-MS torch.

Interference of ^{176}Lu on ^{176}Hf is corrected by measuring the intensity of the interference-free ^{175}Lu isotope and using $^{176}Lu/^{175}Lu = 0.02669$ [49] to calculate $^{176}Lu/^{177}Hf$. Similarly, the interference of ^{176}Yb on ^{176}Hf has been corrected by measuring the interference-free ^{172}Yb isotope and using $^{176}Yb/^{172}Yb$ to calculate $^{176}Yb/^{177}Hf$. The appropriate value of $^{176}Yb/^{172}Yb$ was determined by spiking the JMC475 Hf standard with Yb and finding the value of $^{176}Yb/^{172}Yb$ (0.58669) required to yield the value of $^{176}Hf/^{177}Hf$ obtained on the pure Hf solution. Detailed discussions regarding the overlap corrections for ^{176}Lu and ^{176}Yb are provided in Pearson et al. [50]. Precision and accuracy obtained on the $^{176}Hf/^{177}Hf$ ratio are illustrated by analyses of standard zircons in Griffin et al. [48] and Pearson et al. [50]. The typical 2SE precision on the $^{176}Hf/^{177}Hf$ ratios presented here is about 0.00002, which is equivalent to +0.7 eHf unit. The Mud Tank and Temora zircon were used as independent control on reproducibility and instrument stability. Most of the data and the mean value are within 2 s.d. of the recommended values reported for Mud Tank [$^{176}Hf/^{177}Hf = 0.282522 \pm 42$ (2 s.d.)], [51]) and Temora reference material (0.282680 ± 15; [52]).

In order to calculate εHf values, the chondritic values of Bouvier et al. [53] were adopted: $^{176}Lu/^{177}Hf$ (Chondrite Uniform Reservoir (CHUR), today) = 0.0336, $^{176}Hf/^{177}Hf$ (CHUR, today) = 0.282785, and the decay constant for ^{176}Lu of 1.865 x 10^{-11} yr^{-1} ([54]). To calculate model ages (T_{DM}) based on a depleted-mantle source, we assume that the depleted mantle (DM) reservoir developed from an initially chondritic mantle is complementary to the crust extracted over time. T_{DM} ages, which are calculated using the measured $^{176}Lu/^{177}Hf$ of the zircon, can only give a minimum age for the source material of the magma from which the zircon crystallized. Therefore, we have also calculated a "crustal" model age ($T_{DM}{}^{C}$ in data tables) for each zircon that assumes its parental magma was produced from an average continental crust ($^{176}Lu/^{177}Hf = 0.015$, Geochemical Earth Reference Model database, http://www.earthref.org/), which was derived from a depleted mantle.

3.5. Geochronometry

3.5.1. U-Pb Dating by LA-ICP-MS

Zircon U-Pb ages were measured by using an Agilent 7700 quadrupole ICP-MS attached to a Photon Machines Excimer 193 nm laser system. The analyses were carried out with a beam diameter of 50 μm with 5 Hz repetition rate and energy of 8 J/cm^2. The analytical procedures for the U-Pb dating

have been detailed previously [55]. A very fast scanning data acquisition protocol was employed to minimize signal noise. Data acquisition for each analysis was 3 min (1 min background, 2 min signal). Ablation was carried out in He to improve sample transport efficiency, provide more stable signals, and give more reproducible U/Pb fractionation. Provided that constant ablation conditions are maintained, accurate correction for U/Pb fractionation can then be achieved.

Sample analyses were bracketed by pairs of analyses of the GEMOC GJ-1 zircon standard [47]. The other well-characterized zircon standard 91500 was analyzed within the run as an independent control on reproducibility and instrument stability (see data tables). U-Pb ages were calculated from the raw signal data by using the online software package GLITTER (version 4.4.4, ARC National Key Centre, Sydney, Australia, www.glitter-gemoc.com; [56]). GLITTER calculates the relevant isotopic ratios for each mass sweep and displays them as time-resolved data. This allows isotopically homogeneous segments of the signal to be selected for integration. GLITTER then corrects the integrated ratios for ablation related fractionation and instrumental mass bias by calibration of each selected time segment against the identical time segments for the standard zircon analyses.

The common-Pb correction procedure of Andersen [57] was employed and the analyses presented here have been corrected assuming recent Pb-loss with a common-Pb composition corresponding to present-day average orogenic Pb as given by the second-stage growth curve of Stacey and Kramers [58] for $^{238}U/^{204}Pb=9.74$. No correction has been applied to analyses that are concordant within 2σ analytical error in $^{206}Pb/^{238}U$ and $^{207}Pb/^{235}U$ or which have less than 0.2% common lead.

3.5.2. (U-Th)/He Thermochronology

The age of eruption of the zircon host basalt was determined by (U-Th)/He thermochronology. This method, when applied to zircon, has a closure temperature of ~180 °C (for cooling rate of 10 °C/Ma, ~60 μm diameter diffusion domain equivalent sphere radius, [59]). In the simplest scenario (i.e., simple cooling without subsequent reheating), the ages measured by this method can be interpreted as true 'eruption ages' recording the passage of zircon-bearing magma to the surface and associated cooling. It is important to note that the traditionally used zircon U-Pb geochronology has a closure temperature in excess of ~900 °C and records the time of zircon crystallization in the magma chamber as well as provides a maximum limit for the eruption age, but it cannot directly date the eruption age.

The (U-Th)/He dating of zircon was conducted at the University of Waikato (New Zealand) by following the protocols described in Danišík et al. [60,61]. The large zircon megacrysts (mm–cm sized) could not be fit into the Nb microtubes (i.e., cylinders ~0.9 mm long, with internal diameter of ~0.6 mm) and were, thus, first abraded (thereby removing the uppermost ~30 microns of the surface) using an air-abrasion cell with pyrite as abrasion medium. This step circumvented the need of alpha ejection correction ([62]). Abraded megacrysts were then crushed in a steel mortar. The 60–150 μm fraction was separated using sieves and cleaned in an ultrasonic bath with ethanol. Clean shards (3–5 per sample) were individually loaded into Nb microtubes, degassed at ~1250 °C under ultra-high vacuum by using a diode laser, and analyzed for ^4He by isotope dilution on a Pfeiffer Prisma QMS-200 mass spectrometer. Following He measurements, the zircon shards in Nb microtubes were spiked with ^{235}U and ^{230}Th, and dissolved in hydrofluoric, nitric, and hydrochloric acids. The solutions were analyzed by isotope dilution for U and Th and by external calibration for Sm on a Perkin-Elmer SCIEX ELAN DRC II ICP-MS (PerkinElmer, Inc., Waltham, MA, USA). The total analytical uncertainty (TAU) was calculated as the quadratic addition on He and weighted uncertainties on U, Th, Sm, and He measurements and is typically ~2% (1σ). The raw zircon (U-Th)/He ages were not corrected for alpha ejection (Ft correction) given the abrasion step described above. Replicates (3 to 5 per sample) with associated uncertainties were used to calculate the geometric mean ([63]) and error-weighted standard deviation as representative eruption age for each sample. Replicate analyses of the Fish Canyon Tuff zircon (n = 18) measured over the period of this study as an internal standard yielded a mean (U-Th-Sm)/He age of 28.2 ± 0.6 Ma, which is in excellent agreement with the (U-Th-Sm)/He age of

the Fish Canyon Tuff zircon mineral standard dated at 28.3 $\pm$ 1.3 Ma [64]. All replicates in each sample overlap within 1σ error bars and total analytical errors for individual replicates are significantly below 5%, which is typical for zircon dating procedures.

3.6. $\delta^{18}O$ Isotopic Analyses

Zircons were analyzed by laser fluorination at the University of Wisconsin, Madison. Zircon concentrates were prepared by standard crushing as well as gravimetric and magnetic techniques and soaked in cold HF overnight to remove radiation-damaged domains and contamination Bulk samples of ~2 mg were pre-treated in BrF_5 overnight, fluorinated by laser heating with a 32 W CO_2 laser operating at a wavelength of 10.6 μm, and analyzed by a gas-source mass spectrometer. Data are standardized against multiple analyses of the UWG-2 garnet standard performed on the same day ($\delta^{18}O$ = 5.80‰VSMOW, [65,66]).

4. Results

4.1. Zircon Crystal Morphology and CL Zonation

Morphological studies were done on intact zircon grains as well as by CL after the crystals had been cut and polished to expose their centers. The recognition of the dominant forms, {100} prism and {101} bipyramid, as well as less pronounced {110} prisms and {211} pyramids in each crystal allows for discrimination of zircon morphological types by using the Pupin [67] classification. On the basis of empirical observations, Pupin [67] argued for a relationship between zircon morphology and the composition of the medium in which the zircon crystallized. Those crystallizing from a peraluminous melt are dominated by {211} pyramids and those crystallizing from peralkline melts are dominated by {101} pyramids. The alkalinity index [Al/(Na+K)] is, thus, designated as index A. The temperature of the growth medium (index T) is the dominant factor in controlling the relative development of prism faces with higher temperatures favoring {100} prisms and lower temperatures favoring {110} prisms.

RVP zircon xenocrysts occupy a narrow range of forms on the Pupin [67] typological correlation diagram and fall into two categories: (1) those dominated by the {100} prism and {101} bipyramid belonging to subgroup J5 and (2) those with additional moderately developed {110} prisms and {211} dipyramids belonging to subgroups S19–20 and S24–25. There is no evidence in CL images to suggest that rapid changes in the magma composition or temperature took place during zircon crystallization. Both morphological populations suggest crystallization in an alkaline environment at temperatures of 800–900 $\pm$ 50 °C.

All zircon display strong, primary, magmatic oscillatory growth zoning when imaged by CL (Figure 7), which is a reflection of the non-equilibrium conditions during crystallization [68]. Oscillatory growth areas are very fine with bands on the order of <1–25 μm (Figure 7a,b). A number of grains also display distinctive sector zoning upon which the oscillatory zoning is imposed (Figure 7c–e). Zonation patterns are generally very sharp and crystallographically-controlled. With the exception of one grain, all zircon are non-metamict, unaltered, and do not contain relict cores, which confirms their primary igneous origin. Studies by Witter et al. [69] also found RVP zircon to have negligible radiation damage with time-integrated self-irradiation doses on the order of 10^{16} alpha-decay events/gram (α/g) (note that detectable radiation damage requires a minimum of 0.1–0.2 × 10^{18} α/g). One grain (BL53-1, Figure 7f) contains a core that is black in CL and does not display any discernible zoning pattern in either CL, BSEI, or optically. Limited yet distinct magmatic zoning is observed in BSE images of RVP zircon. However, when the CL and BSE images can be compared, dark regions in CL correspond to bright areas (highest mean atomic weight) in BSE images. Chemical analyses of the individual zones reveal Th and U to be the most important influence, measurable by EMPA, on the observed zonation patterns—regions rich in Th + U are darkest in CL (both sector and oscillatory zoning) and brightest in BSE images. Optically, zones enriched in Th + U are darker in color and range from dark orange-brown to dark red.
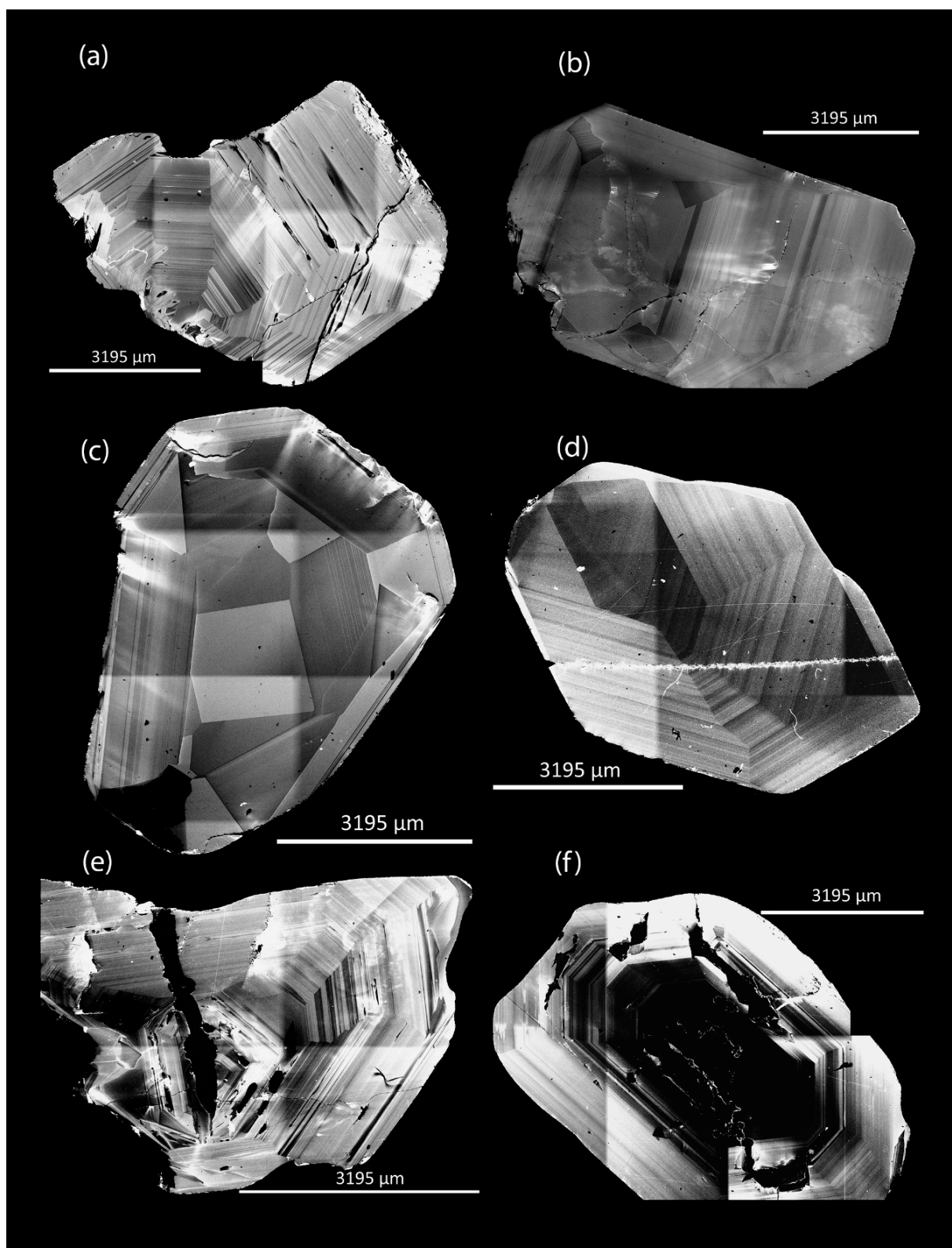
Figure 7. Cathodoluminescence images of RVP zircon xenocrysts showing both oscillatory and sector zonation. Darker zones are enriched in Th, U, and REE: (**a**) concentric zoning in BC43-2, (**b**) concentric zoning in PT49-2, (**c**) sector zoning in PT48-3, (**d**) sector and concentric zoning in BL54-3, (**e**) sector and concentric zoning in BL53-2, and (**f**) dark, CL-inactive core in BL53-1.

These results are in direct contrast to those presented by Cong et al. [23] for six alluvial zircon from an unknown locality in the RVP. Cong et al. [23] indicate that none of the zircon display oscillatory magmatic zoning in CL images and, that in BSE images, the samples are homogeneous. Cathodoluminescence images presented in the Cong et al. [23] study show very weak growth zoning, which is contrary to statements made within the text. In total, more than 50 zircons from the RVP deposits were examined by CL imaging in this study and all showed strong growth zoning. This discrepancy between the two sample sets may simply be the result of incorrect settings during CL imaging by Cong et al. [23]. However, the authors later use these results incorrectly as evidence for thermal homogenization of the zircons in the mantle.

4.2. Zircon Chemistry

Average EMPA data are shown in Table 1 and representative trace element data (ppm) are shown in Table 2. Rim and core analyses are noted when applicable. Figure 8 depicts box plot diagrams for relevant trace elements (a) and ratios (b) in zircon from each locality. Rare-earth element (REE) data were normalized to C-1 chondrite values [70] and plotted on logarithmic multi-element diagrams (La-Lu, Figure 9). Figure 10 depicts the chondrite-normalized trace element spidergram for the RVP zircon (in shaded orange). Data from Cong et al. [23] as well as for zircon from a variety of rock types [5].

Table 1. Average EMPA analyses for RVP zircon xenocrysts.

Sample	BC45	BC46-1	BC46-2	BS47	PT48-1	PT48-2	PT48-3	PT49-1	PT49-2	PT50-1	PT50-2	PT50-3
n *	6	7	7	8	7	4	10	8	7	8	7	7
HfO_2	0.74	0.72	0.80	0.69	0.74	0.77	0.73	0.77	0.80	0.71	0.76	0.79
ZrO_2	66.87	66.04	66.57	66.58	67.04	66.67	67.07	67.50	67.52	67.46	67.39	67.34
Y_2O_3	0.04	0.01	0.03	0.10	0.02	0.03	0.06	0.02	0.03	0.03	0.02	0.03
ThO_2	0.01	0.00	0.01	0.01	0.00	0.01	0.01	0.01	0.01	0.00	0.00	0.01
UO_2	0.01	0.00	0.00	0.02	0.01	0.02	0.01	0.01	0.00	0.01	0.01	0.01
SiO_2	32.34	31.69	32.05	32.62	32.47	32.38	32.49	32.35	32.26	32.32	32.30	32.22
Total	100.01	98.47	99.46	100.01	100.28	99.86	100.37	100.66	100.62	100.53	100.47	100.40
Sample	**BL51-1**	**BL51-2**	**BL52**	**BL53-1**	**BL53-2**	**BL54-1**	**BL54-2**	**BL54-3**	**BL55-1**	**BL55-2**	**BL55-3**	**BL55-4**
n *	6	6	8	16	10	10	5	11	5	6	7	8
HfO_2	0.79	0.72	0.69	0.75	0.73	0.71	0.72	0.75	0.75	0.71	0.71	0.70
ZrO_2	67.66	67.84	68.17	65.79	66.31	66.04	65.80	65.39	66.93	67.20	66.98	67.11
Y_2O_3	0.03	0.04	0.07	0.11	0.03	0.03	0.04	0.17	0.08	0.03	0.06	0.05
ThO_2	0.01	0.00	0.01	0.05	0.01	0.01	0.01	0.07	0.01	0.01	0.01	0.01
UO_2	0.01	0.01	0.01	0.04	0.01	0.01	0.01	0.05	0.03	0.02	0.01	0.01
SiO_2	32.08	32.06	31.99	32.67	32.68	32.38	32.30	32.26	32.28	32.27	32.27	32.35
Total	100.58	100.67	100.94	99.41	99.78	99.19	98.88	98.69	100.07	100.24	100.04	100.23

n * = number of analyses.

Table 2. Average trace element composition, ratios, and sums (ppm) of RVP zircon xenocrysts.

Locality (Code)	Bokeo Clas (BC)			Bei Srok (BS)	Phum Throm (PT)					BoLoei (BL)	
Sample # (n) *	45 (5)	46-1 (4)	46-2 (4)	47 (5)	49-1 (4)	49-2 (4)	50-1 (4)	50-2 (4)	50-3 (3)	53-1 (3)	53-2 (4)
HfO_2 wt %	0.73	0.71	0.80	0.68	0.78	0.79	0.71	0.76	0.80	0.75	0.72
Hf wt %	0.62	0.60	0.67	0.58	0.66	0.67	0.60	0.64	0.68	0.64	0.61
P	58	47	51	91	34	43	51	51	54	53	47
Ti	5.1	4.5	3.7	7.7	3.1	3.1	4.6	3.7	3.8	3.8	4.0
Nb	4.0	1.7	2.3	11.7	1.3	2.0	2.7	2.4	3.2	3.9	2.5
Ta	1.7	0.9	1.3	3.3	0.6	1.1	1.2	1.3	1.6	1.8	1.0
Pb^{204}	1.05	1.16	1.02	1.48	0.97	1.27	1.19	1.18	1.61	1.58	1.28
Pb^{206}	0.05	0.05	0.02	0.13	0.06	0.07	0.03	0.03	0.06	0.18	0.04
Pb^{207}	0.03	0.02	0.02	0.04	0.02	0.02	0.00	0.02	0.03	0.01	0.04
Pb^{208}	0.02	0.06	0.01	0.02	0.02	0.03	0.02	0.01	0.07	0.02	0.01
Th	42	19	13	168	9	17	25	25	30	51	22
U	83	41	39	187	23	43	55	58	61	90	42
Th/U	0.46	0.46	0.33	0.88	0.35	0.35	0.43	0.44	0.38	0.54	0.41
Nb/Ta	2.2	2.0	1.8	3.5	2.3	2.0	2.2	1.8	2.1	2.1	2.4
Yb/Sm_N	71	77	86	25	83	79	59	67	97	52	79
Lu/Gd_N	20	21	24	7	23	22	15	19	28	13	20
Y/Hf	0.00	0.00	0.00	0.00	0.00	0.00	0.00	0.00	0.00	0.00	0.00
Eu/Eu^*_N	1.00	1.01	0.99	0.99	1.04	1.00	1.00	1.03	0.95	1.02	0.99

Table 2. *Cont.*

Locality (Code)	Bokeo Clas (BC)			Bei Srok (BS)	Phum Throm (PT)					BoLoei (BL)	
Sample # (n) *	45 (5)	46-1 (4)	46-2 (4)	47 (5)	49-1 (4)	49-2 (4)	50-1 (4)	50-2 (4)	50-3 (3)	53-1 (3)	53-2 (4)
Y	365.9	150.4	169.9	921.8	119.7	196.1	259.3	245.1	222.7	299.8	206.2
La	bdl	bdl	bdl	bdl	bdl	bdl	bdl	bdl	bdl	bdl	bdl
Ce	1.7	0.7	0.9	5.3	0.6	1.0	1.0	1.1	1.2	2.3	1.2
Pr	0.1	0.0	0.0	0.2	0.0	0.0	0.0	0.0	0.0	0.0	0.0
Nd	0.9	0.3	0.3	3.8	0.3	0.6	0.5	0.7	0.3	0.6	0.3
Sm	1.7	0.6	0.6	6.7	0.6	1.0	1.2	1.3	0.7	1.2	0.8
Eu	1.3	0.5	0.5	4.6	0.4	0.7	0.9	0.9	0.6	1.0	0.6
Gd	8.8	3.5	3.4	29.7	2.8	4.8	6.4	6.1	4.2	7.4	4.8
Tb	2.9	1.1	1.2	8.8	0.9	1.5	2.1	1.9	1.5	2.4	1.6
Dy	37	15	16	103	12	19	27	24	20	31	21
Ho	12	5	6	30	4	7	9	8	7	10	7
Er	55	23	26	120	18	30	39	37	35	43	30
Tm	11	5	5	20	4	6	7	7	7	8	6
Yb	100	44	54	166	36	57	63	70	69	68	52
Lu	18	8	10	25	7	11	11	13	13	12	9
ΣREE	250	107	124	524	86	139	168	172	160	186	135
ΣREE+Y	616	257	294	1446	205	335	427	417	383	486	341
Ce/Ce*$_N$	18	11	23	24	14	21	19	13	38	31	37

bdl = below detection limit.
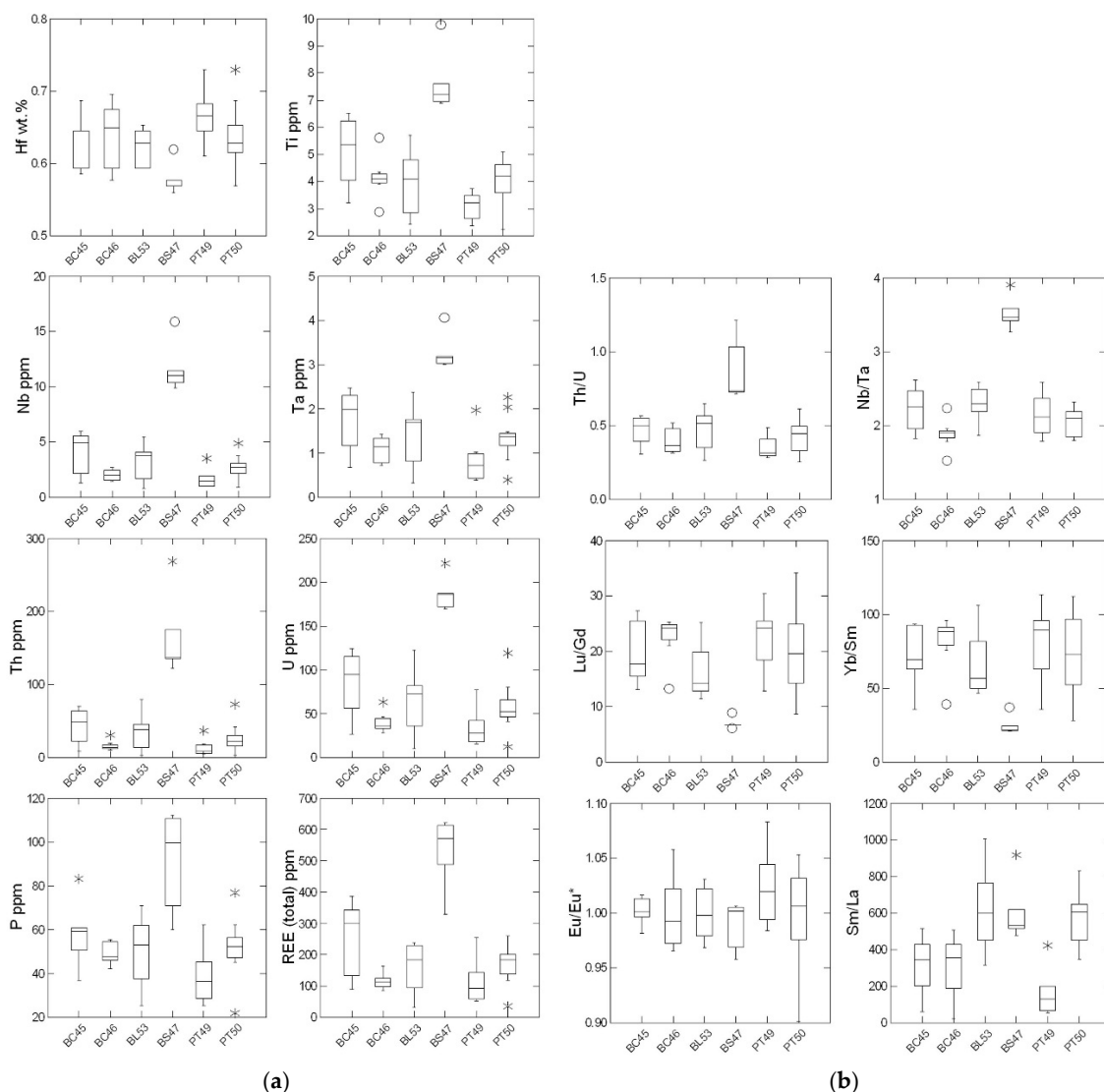

(**a**)   (**b**)

Figure 8. Boxplot diagrams for relevant trace element (**a**) and trace element ratios (**b**) in RVP zircon xenocrysts. The vertical line and whiskers represent the range in the data values with the horizontal line representing the median of the data set. The box is defined by the first and third quartiles.
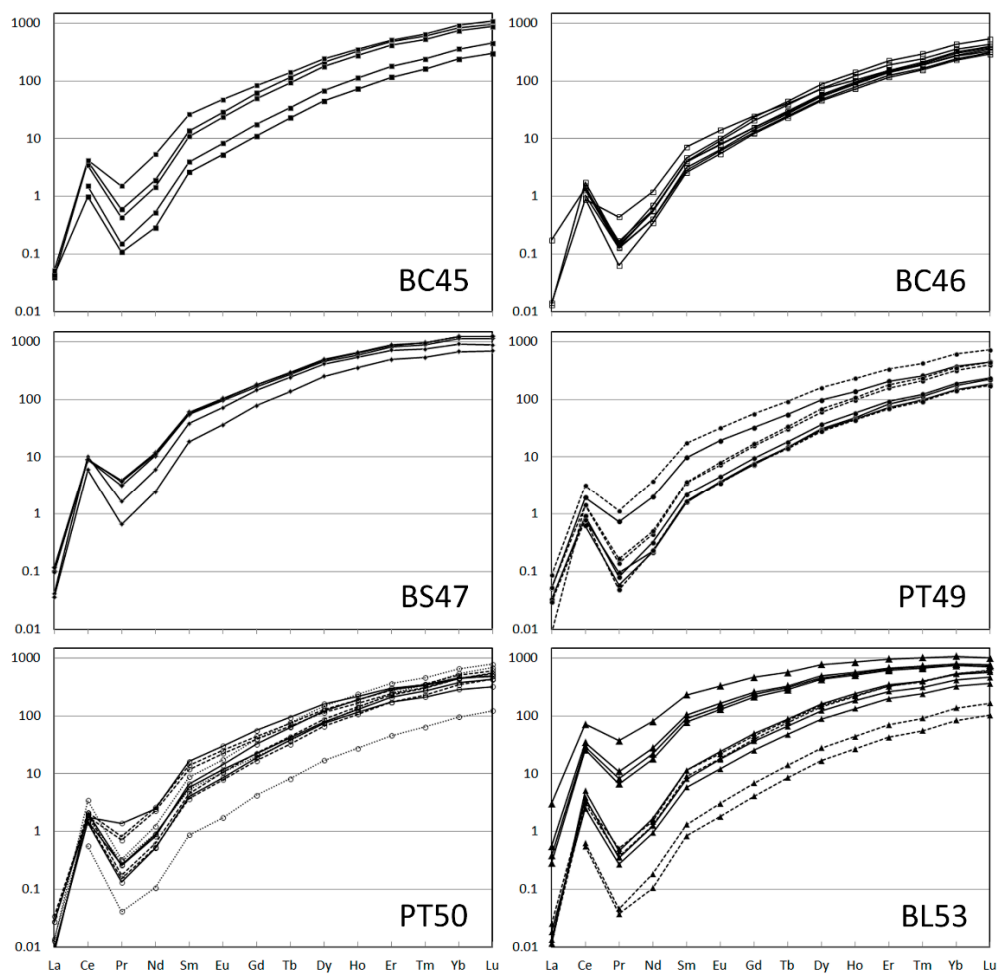
Figure 9. Average chondrite-normalized REE patterns for RVP zircon xenocrysts.
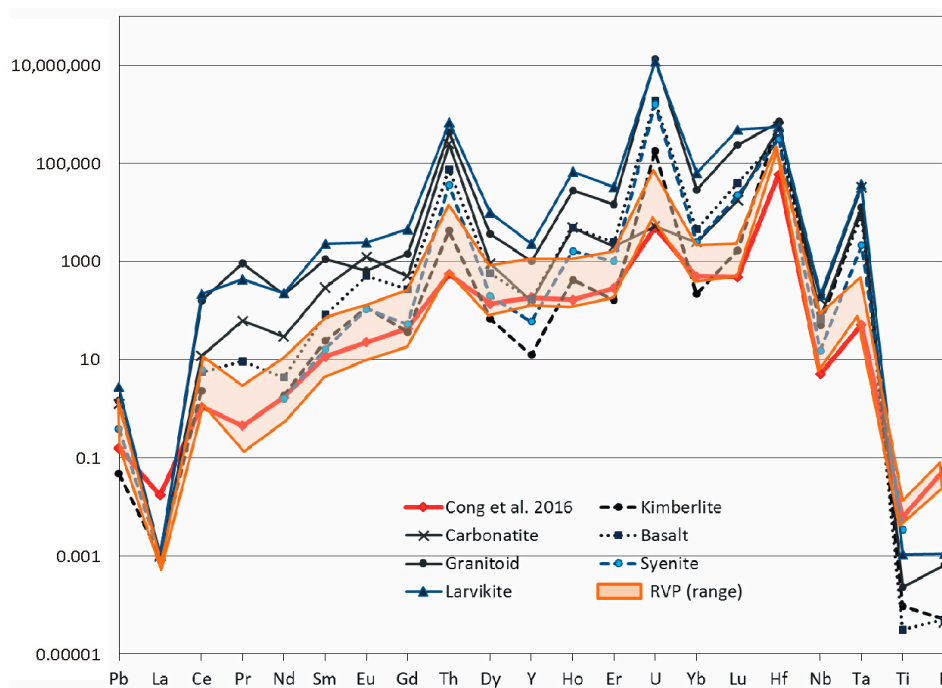

Figure 10. Chondrite-normalized trace element spidergram for zircon from the RVP (orange shaded region) including average data from Cong et al. (red [23]) and zircon from other rock types [5].

Electron microprobe analysis of the zircon xenocrysts gave major element compositional ranges of SiO_2 from 30.93 to 32.87 wt % and ZrO_2 65.06 to 68.36 wt %. Hafnium contents range from 0.66 to 0.86 wt % with an average of 0.74 wt % and do not show significant variation from core to rim. Y_2O_3 contents range up to 0.23 wt % (average: 0.05 wt %). Zircon from Bei Srok has lower HfO_2 than other RVP zircon (range: 0.66 to 0.73 wt %, average: 0.68 wt %). The Zr/Hf ratios (elemental) range from 66 to 88 (average: 79), which is higher than expected for mantle zircon (Zr/Hf = 60–68, Pupin [71]). Zircon from the RVP show wide variations in Ti, Nb, Ta, U, Th, P, Y, and REE contents between both grains and localities. In general, all RVP zircon show heavy REE (HREE) enrichment, have a positive Ce anomaly, and lack a negative Eu anomaly with ΣREE+Y, U, Th, and Ti contents exhibiting a decrease from core to rim in most samples. No compositional difference is observed between morphological types of the xenocrysts. Two distinct compositional populations exist: (1) the main population of RVP zircon from Bokeo Clas, Phum Throm, and BoLoei and (2) zircon from Bei Srok, which have higher overall trace element concentrations than the main RVP population.

Zircon from the main population have trace element concentrations as follows [ppm range (average)]: P 22–88 (average 51), Ti 1.6–6.5 (average 3.7), Nb 0.8–6 (average 2.6), Ta 0.3–3 (average 1.3), Th 2.6–135 (average 28), U 10–157 (average 55), and Y 43–560 (average 227). Average Nb/Ta and Th/U ratios are 2.11 and 0.44, respectively (Figure 5b). The bulk of the zircon are characterized by low ΣREE contents (31–386 ppm, average 154 ppm), which is typical of xenocrysts from alkaline mantle sources [5]. Total REE(+Y) contents decrease from the core to the rim in all samples. The chondrite-normalized REE patterns (Figure 10) show strong light REE (LREE) depletion, which is a pronounced positive Ce anomaly (Ce/Ce*$_N$ = 11–38, average 27, Eu/Eu*$_N$ = 1, and heavy REE (HREE) enrichment characterized by a steep, straight slope with Yb/Sm$_N$ ranging from 28–113 (average 75) and Lu/Gd$_N$ = 9–34 (average 20). Normalized Ce and Eu anomalies were calculated as $Ce/Ce*_N = \frac{Ce}{\sqrt{La \times Pr}}$ and Eu/Eu*$_N$ $= \frac{Eu}{\sqrt{Sm \times Gd}}$, respectively.

Zircon from Bei Srok (BS47) has higher overall trace element contents as compared to those from other RVP localities [Figure 8, range (average) ppm]: P 60–112 (average 91), Ti 7–10 (average 8), Nb 10–16 (average 12), Ta 3–4 (average 3), Th 123–269 (average 168), U 170–221 (average 187), and Y 574–1076 (average 922). Total REE contents range from 328 to 621 ppm (average 524 ppm) and decrease from core to rim. Bei Srok zircon has significantly higher Nb/Ta (average 3.53) and Th/U (average 0.88) as compared to zircon from BC, PT, and BL (Figure 9b). The chondrite-normalized REE pattern for BS zircon (Figure 9) shows strong LREE depletion with a pronounced positive Ce anomaly (Ce/Ce*$_N$ = 13–38, average 24), Eu/Eu*$_N$ = 0.99, and middle REE (MREE)/HREE enrichment characterized by a steep, slightly concave-down curvature with Yb/Sm$_N$ = 21–37 (average 25) and Lu/Gd$_N$ = 6–9 (average 7).

Ti-in-Zircon Thermometer

Watson and Harrison [72] and Watson et al. [73] used high-pressure/high-temperature experimental methods coupled with analyses of natural zircons to determine the exact relationship between Ti content and crystallization temperature in zircon TiO_2. The resultant Ti-in-zircon thermometer (Equation (1)) has the capability to provide temperature with a precision of ± 5 °C depending on the Ti concentration and the analytical method employed [73].

$$T\ (°C)_{zircon} = [5080/(6.01 - \log(Ti_{ppm})] - 273 \tag{1}$$

A number of limiting factors must be considered when utilizing the Ti-in-zircon thermometer including the variation of TiO_2 or SiO_2 activity in the melt, the pressure fluctuation, changes in the Ti content of the zircon as a result of solid state diffusion or post-crystallization alteration, and the assumption that the temperature dependence of Ti in zircon is an equilibrium process and obeys Henry's Law [74]. Cherniak and Watson [75] demonstrated that Ti is strongly retained by the zircon

structure in both anhydrous (1 atm) and H_2O-CO_2-bearing (1.1–1.2 GPa) systems at temperatures between 1350 and 1550 °C.

Titanium contents in the analyzed zircon are all above the detection limit (0.1 ppm) and range from 2 to 10 ppm (Table 3). All zircon are primary magmatic phases with oscillatory zonation, which is the result of intrinsic non-linear feedback between the parental melt and the growing crystal [68]. Although this zonation suggests local non-equilibrium during growth, which is a result of the continuous process of depletion and replenishment of solute at the crystal-melt boundary, there is no evidence for large-scale disequilibrium due to extrinsic mechanisms in the system. This indicates that Ti contents in the zircon are a primary magmatic feature. In addition, there is no evidence for metamictization or alteration which could be responsible for Ti diffusion. As such, the temperatures obtained by the Ti-in-zircon thermometer are considered representative of the difference in relative crystallization temperatures between zircon from the RVP localities.

Table 3. Ti-in-zircon temperatures for RVP zircon xenocrysts.

Locality	Sample # (n) *	Ti ppm $\pm$ 2 SD	T °C $\pm$ 2 SD
Bokeo Clas	45 (5)	5.07 $\pm$ 2.83	682 $\pm$ 46
-	46-1 (4)	4.53 $\pm$ 1.45	675 $\pm$ 23
-	46-2 (4)	3.75 $\pm$ 1.20	661 $\pm$ 26
Bei Srok	47 (5)	7.68 $\pm$ 2.38	718 $\pm$ 24
Phum Throm	49-1 (4)	3.05 $\pm$ 1.04	646 $\pm$ 24
-	49-2 (4)	3.14 $\pm$ 1.07	648 $\pm$ 26
-	50-1 (4)	4.64 $\pm$ 0.81	677 $\pm$ 14
-	50-2 (4)	3.67 $\pm$ 0.36	660 $\pm$ 7
-	50-3 (3)	3.81 $\pm$ 2.87	659 $\pm$ 63
BoLoei	53-1 (3)	3.77 $\pm$ 1.23	661 $\pm$ 26
-	53-2 (4)	4.03 $\pm$ 3.52	662 $\pm$ 69

* n = number of analyses, SD = standard deviation.

Average Ti-in-zircon temperatures are 663 $\pm$ 28 °C (range: 601–739 °C, Table 3). In general, there is a decrease in the calculated temperature from core to rim in all samples with ΔT ranging from 10–55 °C. Wider variation in temperature between core and rim may simply reflect the larger size of the zircon grains themselves, which is a possible reflection of residence time within the parental melt. No difference in calculated temperatures is observed between the various morphological types, which is contrary to what is predicted based on Pupin's T versus A diagram [67]. Temperatures based on morphological studies suggest crystallization at 800 to 900 °C, which is significantly higher than that predicted by Ti-in-zircon temperatures. The lower T for Ti-in-zircon results than predicted for natural zircon may result from pressure and Ti^{4+} substitution effects [76]. The relatively low Ti-in-zircon for RVP samples may reflect the likely high-pressure mantle origin of these xenocrysts, which has also been suggested for kimberlite zircons [77].

4.3. Geochronology Results

U-Pb age dates were obtained for 11 zircon grains from the four mining regions with three to nine analyses per grain (Table S1). All samples lack any significant U-Pb age differences between core and rim, which confirms the lack of inherited cores and a single growth event for all the zircon. The young zircon xenocrysts are depleted in ^{207}Pb and subsequently ^{207}Pb/^{235}U ages are very poor with large associated errors. As a result, only ^{206}Pb/^{238}U is reported in this case (Table 4). Weighted mean ^{206}Pb/^{238}U ages range from 0.88 $\pm$ 0.22 Ma (PT50) to 1.56 $\pm$ 0.21 Ma (PT49) at the 95% confidence level (1σ error, Table 4). Seven U-Pb ages determined by ID-TIMS on RVP zircon during a gemological study [45] gave an average age of 0.92 $\pm$ 0.07 Ma (range: 0.83–1.03 Ma), which is in agreement with analyses in this study (Table 4). Analyses of a zircon inclusion in corundum from the BL deposit gave a U-Pb age of 0.855 $\pm$ 0.098 Ma, which suggests a temporal, if not a genetic, relationship between the two xenocrystic phases [12]. Similar age ranges are noted for zircon xenocrysts from Eastern

Gondwana margins including Western Cambodia (Table 4). Fission track dating of zircon from Bokeo by Carbonnel et al. [78] yielded ages ranging from 1.10–1.41 Ma, which is also in agreement with the ages from this study.

Table 4. U-Pb, fission track and (U-Th)/He age dates for ZIP xenocrysts.

Locality	U-Pb	Fission Track/(U-Th)/He	Reference
Ratanakiri Volcanic Province (This Study)	-	-	-
Bokeo Clas (BC45)	0.98 ± 0.12	-	This study
Bokeo Clas (BC46)	1.07 ± 0.19	0.91 ± 0.02	-
Bei Srok (BS47)	1.143 ± 0.073	1.02 ± 0.02	-
Phum Throm (PT49)	1.56 ± 0.21	0.93 ± 0.02	-
Phum Throm (PT50)	0.88 ± 0.22	1.02 ± 0.02	-
-	-	0.86 ± 0.02	-
BoLoei (BL53)	0.978 ± 0.054	0.96 ± 0.06	-
-	-	0.96 ± 0.09	-
RVP (unknown locality)	0.92 ± 0.07	-	[45]
-	-	-	-
Pailin, Cambodia	2.74 ± 0.47	2.14 ± 0.02	This study
-	2.27 ± 0.15–2.60 ± 0.20		[78]
-	1.77 ± 0.15–2.0 ± 0.20	-	[79]
Chanthaburi-Trat, Thailand	1.19 ± 0.29–2.22 ± 0.22	0.90 ± 0.04–2.13 ± 0.04	This study
-	2.57 ± 0.20	-	[78]
Dak Nong, Vietnam	1.05 ± 0.05	-	[7]
-	7.13 ± 0.88	-	-
Xuan-Loc, Vietnam	0.57–0.70	-	[78]
-	0.2–0.9	-	-
Ban Huai Sai, Laos	1.14 ± 0.07–1.46 ± 0.06	-	[38]
-	2.4 ± 0.7–4.3 ± 1.0	-	[11]
Penglai, Hainan Island, China	4.4 ± 0.1	-	[80]
-	-	4.06 ± 0.35	[81]
Mingxi, China	1.2 ± 0.1	-	[13]
NE Australia	2.61 ± 0.16–2.92 ± 0.16	-	[10]

A total of 37 crystal shards of zircon crystals from the four mining regions were dated by the (U-Th)/He method (Table S2). Reproducibility of (U-Th)/He ages (ZHe) from each locality (typically 5-6 ages) was excellent with all replicates overlapping within analytical uncertainty. Final ZHe ages, calculated for each locality as error-weighted means and standard deviation as uncertainty, range between 0.86 ± 0.02 and 1.02 ± 0.02 Ma (Table 4). These are slightly younger or overlap with uncertainty via the corresponding U-Pb ages measured by LA-ICP-MS, which represent a minimum time for zircon crystallization in accordance with the closure temperature concept [82] and also confirms the accuracy of both dating methods. The age and similarity of ZHe and U-Pb ages points to an extremely fast cooling of the crystals from magmatic temperatures through the zircon helium closure isotherm and suggests that the dated crystals erupted to the surface approximately in the same time between 1.02 and 0.86 Ma. As with the U-Pb ages, there seems to be no correlation between the ZHe eruption ages and the spatial distribution of dated samples.

4.4. Hf Isotope Signatures

Zircon from the RVP deposits show a moderate range in the Hf isotope composition (Table S3)—the ^{176}Hf/^{177}Hf ratio ranges from 0.282919–0.283065 (average 0.282982 ± 15, n = 20), which corresponds to positive εHf values ranging from 4.77 to 9.92 (average 7.00 ± 0.25). Zircon from Bokeo Clas, Bei Srok, and BoLoei are the most radiogenic with the highest ^{176}Hf/^{177}Hf ratios (BC45 = 0.283065, εHf 9.92, BS47 = 0.283039, εHf 9.01, and BL53 = 0.283021, εHf 8.37), which all exhibit within-grain variation greater than their 2SE uncertainties. While variations in ^{176}Hf/^{177}Hf within single grains are observed, there is no consistent relationship between core and rim compositions.

Estimated minimum model ages (T_{DM}) for the source material range from 260 to 401 Ma with crustal model ages ($T_{DM}{}^C$) ranging from 391 to 633 Ma.

Zircon from Phum Throm (PT) are the least radiogenic and exhibit less within-grain and between-grain variation (Figure 8). The $^{176}Hf/^{177}Hf$ ratio ranges from 0.282919 to 0.282985 (average 0.282964 ± 6) with εHf 4.77–7.11 (average 6.34 ± 0.59). Estimated minimum model ages (T_{DM}) for the source material are higher for PT zircon and range from 372 to 462 Ma (average 403 Ma) with crustal model ages ($T_{DM}{}^C$) ranging from 605 to 754 Ma (average 654 Ma).

4.5. Oxygen Isotope Ratios

Oxygen isotope ratios provide valuable information about the melt from which the zircon crystallized, which often allows for the discrimination between mantle and crustal sources. Values of $\delta^{18}O$ in RVP zircon are homogeneous with $\delta^{18}O$: 4.93 ± 0.05‰ VSMOW (*n* = 5, Table 5). These values are consistent with those obtained by SIMS for zircon megacrysts from an unknown RVP locality: $\delta^{18}O$ = 4.5–5.5‰ VSMOW, weighted mean = 5.0 ± 0.18‰ VSMOW, *n* = 210 [23]. The slow rate of diffusion of ^{18}O in non-metamict zircon, coupled with the large crystal size and primary magmatic compositional zoning indicate the $\delta^{18}O_{zrn}$ to represent initial magmatic values [83,84]. These values are low, but, within the $\delta^{18}O_{zrn}$ range for igneous zircon in high temperature equilibrium with a mantle source ($\delta^{18}O_{zrn}$ = 4.7–5.7‰ VSMOW) and olivine from mantle xenoliths ($\delta^{18}O_{ol}$ = 5.15 ± 0.13‰ [85]). Similarly, RVP $\delta^{18}O_{zrn}$ are lower than those observed for other alkali basalt-hosted zircon xenocrysts in SE Asia including in Western Cambodia at Pailin (5.95 ± 0.02‰), Chanthaburi-Trat and Bo Phloi (Thailand, 5.82–6.16‰, Table 5) and Penglai, Hainan Island (South China, $\delta^{18}O_{zrn}$ = 5.31 ± 0.18‰ [80]). The lower $\delta^{18}O$ values observed in RVP zircon are akin to values observed in zircon from monominerallic anorthoclase xenoliths, which are called anorthoclasites, in alkali basalt at Elie Ness, Scotland (4.49–5.03‰, average 4.78 ± 0.16‰; [86]) and in zircon from kimberlite [77,87]. The $\delta^{18}O_{zrn}$ values for RVP zircon suggest crystallization from a homogeneous igneous reservoir in the SCLM underlying the RVP with little to no contamination by supracrustal lithologies.

Table 5. $\delta^{18}O$ data for xenocrystic zircon from the RVP and Thailand.

Sample	mg	μml	μml/mg	$\delta^{18}O$ raw	$\delta^{18}O$ VSMOW
Cambodia-RVP	-	-	-	-	-
Bokeo Clas, BC46	2.85	32.7	11.5	4.93	4.95
Bei Srok, BS47	3.14	34.8	11.1	4.87	4.89
Phum Throm, PT49	2.82	30.7	10.9	4.99	5.01
Phum Throm, PT50	3.40	36.7	10.8	4.86	4.88
Bo Loei, BL55	3.26	35.1	10.8	4.90	4.92
Cambodia-Pailin	2.97	32.1	10.8	5.93	5.95
Thailand	-	-	-	-	-
Khao Ploi Waen, Chanthaburi-Trat	3.80	41.0	10.8	6.14	6.16
Tok Phrom, Chanthaburi-Trat	3.05	32.3	10.6	5.80	5.82
Bo Phloi, Kanchanaburi	3.46	37.1	10.7	5.86	5.88
Standards	-	-	-	-	-
UWG-2, garnet	3.39	45.6	13.5	5.78	-
UWG-2, garnet	2.29	31.4	13.7	5.79	-
UWG-2, garnet	2.16	28.3	13.1	5.80	-
UWG-2, garnet	2.70	36.0	13.3	5.77	-

* n = 4, x = 5.78, ± 0.02‰ 2 std. dev. Note: Thailand analyses performed under the same analytical conditions as RVP zircon.

5. Discussion

5.1. Classification and Comparisons of RVP Zircon Xenocrysts

The extensive substitution of trace elements (up to 50) into the zircon structure is useful in studies of the compositional variation in igneous zircons as a petrogenetic indicator. Such data can reveal fractionation processes, the nature of source rocks, and provenance of zircons from secondary deposits [5,88–92]. Shnukov et al. [92] and Pupin [93] utilized Hf and Y concentrations to classify magmatic zircons by focusing on early-stage and late-stage magmatic phases from both mantle and crustal rocks of orogenic and anorogenic origins. Belousova et al. [5] analyzed trace element compositions of zircons from nine different igneous rock types ranging from ultramafic to granitic and syenitic in nature as a way to statistically discriminate between zircon populations and assist in the identification of their source regions. The study suggested that compositional variation in HfO_2, Y, Nb, Ta, Lu, Ce/Ce^*_N, ΣREE, Yb/Sm_N, and Th/U are the most useful petrogenetic indicators across the represented range of rock types and that the provenance or parent rock type of a zircon can be determined at confidence levels of 75% or more.

Zircon xenocrysts from the RVP typify zircons that crystallize from a juvenile, Zr-saturated, REE+Y-enriched alkaline magma or melt with low HfO_2 (<0.9 wt %), Y_2O_3 (<0.2 wt %), U, Th, ΣREE (<600 ppm), $Eu/Eu^*_N \approx 1$, and steep, and HREE-enriched REE profiles [4,5,94]. RVP zircon xenocrysts exhibit the depletion of $\Sigma REE+Y$, U, and Th with increasing Yb/Sm_N from core to rim at almost a constant Hf content. Such zoning favors zircon growth as a single growth stage in an alkaline environment rather than growth involving fractional crystallization [22,94,95]. In depolymerized alkaline melts, the partition coefficients for Hf and Zr between zircon and melt are approximately equal over a wide *T* range and melt compositions [22]. As such, crystallization of zircon will not fractionate Zr and Hf significantly, which results in near constant Zr/Hf in the zircon/melt. An accompanying trend of decreasing REE, Y, U, and Th and increasing Yb/Sm_N suggests that RVP zircon crystallized during a single magmatic event with no influx of additional melt components. The lack of a negative Eu anomaly in these zircons also suggests crystallization in a system where plagioclase did not crystallize or at pressures above the plagioclase stability zone (~0.80 GPa in fertile mantle lherzolite [96]), which lends further support to a sodium-potassium-rich melt. Increasing Yb/Sm_N from core to rim may indicate the depletion of the melt in LREE as a result of a co-crystallizing phase (i.e., apatite) or selective absorption of HREE during the crystallization period [94]. RVP zircon xenocrysts found as isolated crystals within the host alkali basalt, contain corroded REE-rich apatite, and REE carbonates as rare inclusions in larger crystals. Lacombe [43] also noted a carbonate mineral within the RVP zircon as a further sink for LREE and a likely growth environment enriched in CO_2.

Utilizing the classification by Pupin [93] based on HfO_2 and Y_2O_3 contents, all RVP zircons plot in field 1c, mantle-derived hawaiite and alkali basalt, which lies within a narrow range of Hf contents and a spread of Y contents (18–2011 ppm). In Shnukov's Y versus Hf diagram, RVP zircons almost entirely fall within the carbonatite field (VII), with rare samples in the alkaline rocks and alkaline metasomatite field (VI) [92]. Such affinities also apply to zircon xenocrysts from nearby Ban Huai Xai, Laos [11], and Pailin, and Cambodia (Piilonen, unpublished data, Figure 11). The statistical classification scheme by Belousova et al. [5] predicts a cabonatitic provenance for almost all RVP zircon xenocrysts in agreement with the Y versus Hf discrimination diagram except for BS47 in which a higher Lu content (>20.7 ppm) suggests an origin from a basaltic parental melt.
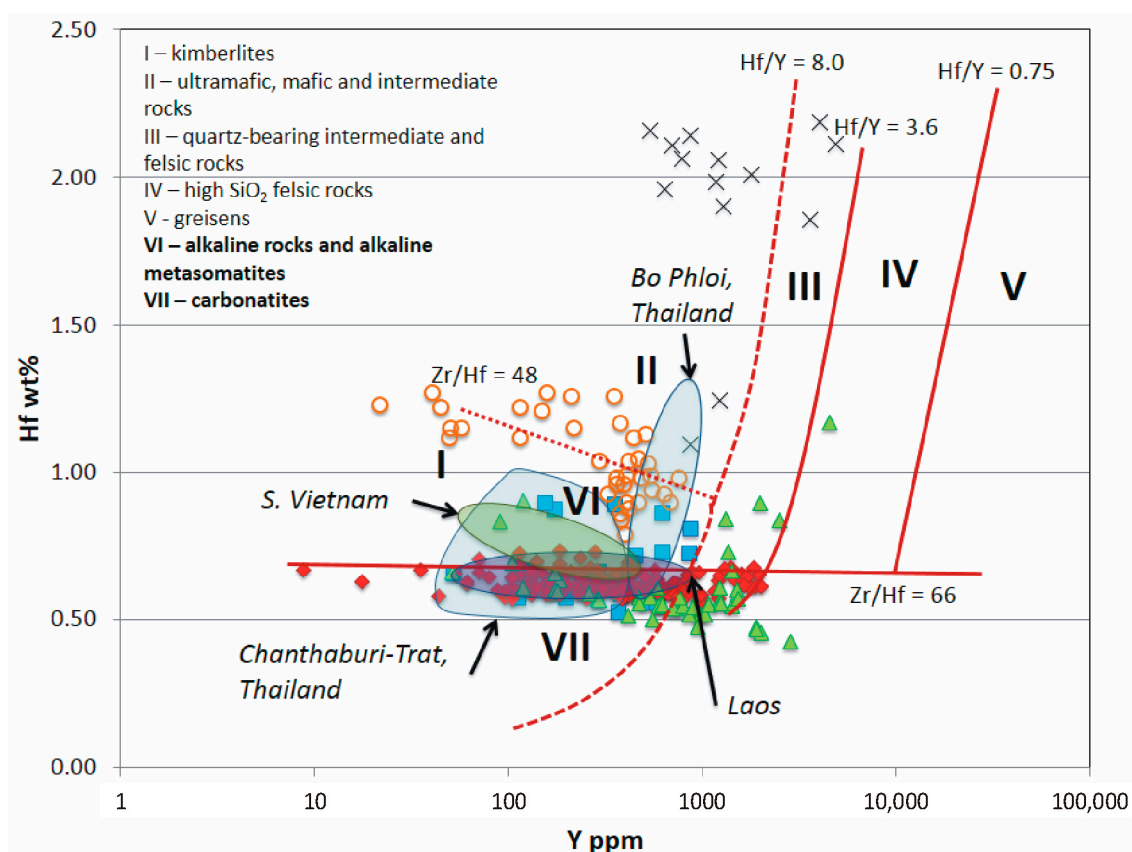
Figure 11. Y versus Hf discrimination diagram for RVP zircon, zircon xenocrysts from ZIP localities, and zircon inclusions in corundum (modified after [92]). Red diamonds: RVP zircon, blue squares: Pailin, Cambodia (Piilonen, unpublished data), blue field: Thailand (Piilonen, unpublished data), green triangles: Australia [11], orange circles: zircon xenocrysts from carbonatites [5], black crosses: zircon inclusions in corundum xenocrysts [10,12,38,97].

Isolated RVP zircon xenocrysts differ from many other zircon xenocryst suites that are commonly spatially associated with corundum xenocrysts either in multimineralic xenoliths or as discrete crystals in heavy mineral separates, e.g., Bo Phloi and Chanthaburi-Trat regions in Thailand (Piilonen, unpublished data, [98,99]), South Vietnam [100], Loch Roag, Scotland [97], and Lava Plains, NE Australia [10,12]. Such zircons associated with corundum, either as xenocrysts or as corundum-hosted inclusions, have consistently higher Hf (>1 wt % and up to 4.5 wt % HfO_2) and often negative Eu anomalies, which suggests evolved, likely peraluminous corundum-bearing sources (Figure 11). Zircon inclusions in blue-green-yellow magmatic corundum xenocrysts (BGY suite) not only show enriched Hf and noticeable negative Eu anomaly but also have enrichments in Y (up to 1 wt % Y_2O_3), U (up to 1 wt % UO_2), Th (up to 2.1 wt % ThO_2), and REE up to 12,060 ppm [11,101–103]. These corundum-hosted zircons are dominated by the {110} prism over the {100} prism unlike the RVP zircon xenocrysts and are a morphology thought to be related to high U, Th, Y, REE, and P contents in the parental melt [104]. Plotted on the Y versus Hf discrimination diagram (Figure 12), the zircon compositions hosted in RVP corundum fall across Type II and III sources (II—ultramafic, mafic, and intermediate rocks, III—quartz-bearing intermediate and felsic rocks).

(**a**)

(**b**)
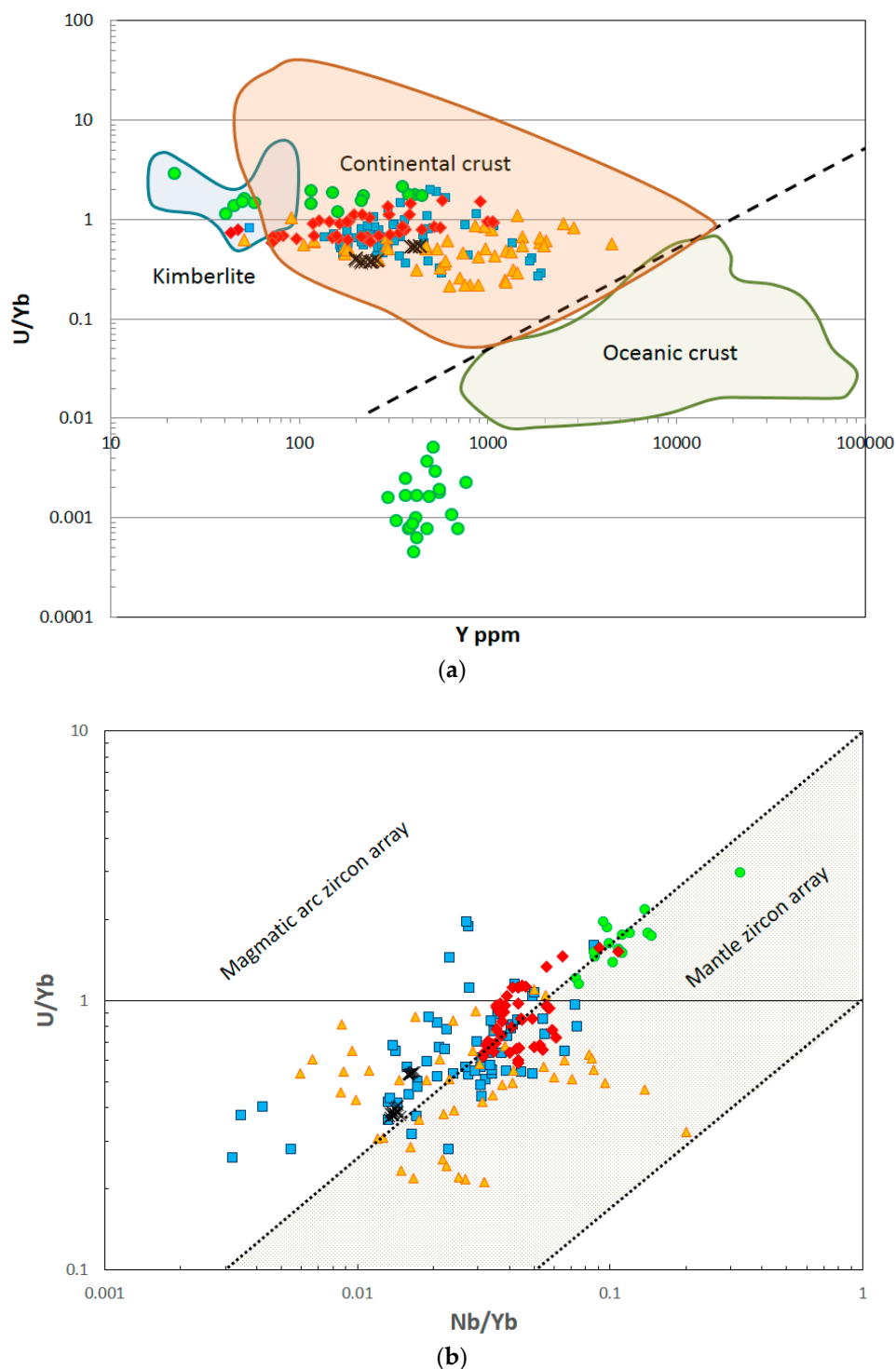
Figure 12. Y versus U/Yb (**a**) and Nb/Yb versus U/Yb. (**b**) Discrimination diagrams for zircon from the RVP (red diamonds, black X's [23]), Thailand (blue squares, Piilonen, unpublished data), other ZIP localities (orange triangles, Australia, Laos, Vietnam [11]), and carbonatites (green circles [5]). Fields for continental and oceanic crust and kimberlite from Grimes et al. [105]. Fields for mantle and magmatic arc arrays from Grimes et al. [106].

5.2. Source Affinities

All RVP zircon xenocrysts have trace element and O-Hf isotopic compositions indicative of a primary, alkaline magma derived from a variably-depleted lithospheric mantle source with

limited supracrustal contamination. Their Hf isotopic compositions lie between those for depleted, juvenile mantle and a chondritic reservoir (CHUR, Figure 13). This supports either (1) a juvenile mantle source mixed with older crustal material or (2) recycled material with a longer crustal residence time. Their Y versus Yb/U are more chemically aligned to continental crust rather than recycled oceanic crust values (Figure 11), which is observed for zircon xenocrysts from other mantle-derived rocks including some kimberlites and carbonatites [105]. The variance in the Hf isotope compositions between RVP samples and within grains (εHf = 4.77–9.92) may, therefore, reflect localized source variation or unmixed crustal or metasomatic components. Griffin et al. [48] suggested that low and variable εHf in some kimberlitic zircon may be due to crystallization from DM-derived or the ocean island basalt (OIB)-type magmas undergoing assimilation/fractionation reactions with a non-radiogenic lithosphere. The SCLM underneath the RVP is a complex region of multiple rift-related and back-arc-related collisional remnants, the Song Ma suture zone, and back margins of the Himalayan collision zone. As the zircon xenocrysts did not crystallize from the host alkali basalt magma, an additional Mantle-derived melt is needed. A DM-derived melt interacting with SCLM underneath the RVP would encounter various reservoirs with non-radiogenic Hf, widely varying ages, and Lu/Hf ratios will result in variable ^{176}Hf/^{177}Hf in the crystallizing zircon.

　　Similarities of U-Pb (0.88–1.56 Ma) and (U-Th)/He ages (0.86–1.02 Ma) yielded by RVP zircon crystals suggest their minimal mantle residence time (0.18–0.86 Ma) and a rapid ascent to the near-surface temperatures facilitated by the alkali basalts. The U-Pb and (U-Th)/He ages, however, are clearly older than the geomagnetic reversal at 0.7 Ma that predates the later, explosive phase of basaltic volcanism in the area [42]. The U-Pb and (U-Th)/He, thus, suggest an earlier onset of basaltic volcanism in the area starting at least at ~1.02 $\pm$ 0.02 Ma. Crystal morphology, compositional zoning, and REE patterns indicate zircon growth from a single magma without fractional crystallization or injection of additional melts.

　　Model Hf ages for RVP zircon give dates significantly older than given by U-Pb and (U-Th)/He methods and correspond to major tectonic events in the SE Asia region. The estimated minimum T_{DM} model ages (333–403 Ma) correspond to the Alleghenian orogeny and suturing of the Indochina and South China blocks (~340 Ma). The older estimated minimum T_{DM}^{C} model ages suggest that the source material for RVP zircon crystallization separated from the depleted mantle around 500–650 Ma during a major crust-building collision between East and West Gondwana to form late Neoproterozoic Pannotia (~650 Ma), which then broke-up in the early Paleozoic (~550 Ma).
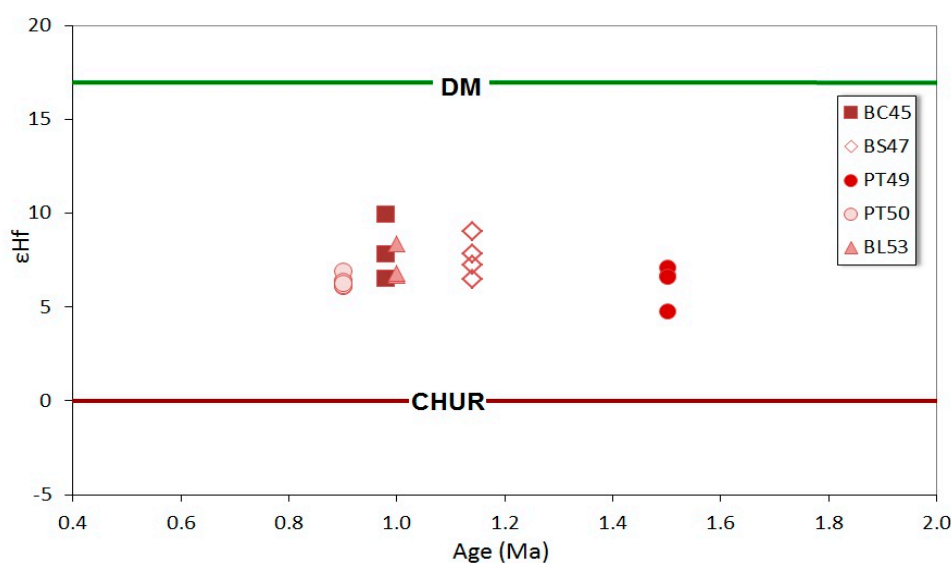

Figure 13. U-Pb Age (Ma) versus εHf for RVP zircon. CHUR: Chondritic uniform reservoir, DM: Depleted mantle.

5.3. Carbonatitic Signatures in Ratanakiri Zircons

Geochemical signatures in RVP zircon suggest that the crystallizing melts had carbonatitic links. Chemical ranges for carbonatite-derived zircons, however, are loosely defined and are much wider than the main carbonatite field (VII) in their Hf-Y discrimination diagram. They also fall within fields (II) ultramafic, mafic, and intermediate rocks as well as (VI) alkaline rocks and alkaline metasomites (Figure 9) [5]. Some zircons analyzed from carbonatitic dikes proved to represent crystallization from a silicate melt instead of a carbonatitic melt and are probably xenocrysts from wall rock contamination [107]. Strict chemical characterization of 'carbonatitic zircons' is clearly complex and partly unreliable [108,109]. Saava et al. [109] surveyed more than 100 carbonatitic zircons and found only 45% could be assigned to a carbonatitic source and that large compositional variation existed between both individual grains and localities. This variation may represent a constantly-evolving carbonatitic melt and its interaction with co-magmatic silicate sources or reflect variable generation in continental carbonatites from the SCLM and, in cases of oceanic island carbonatites, generation in the asthenosphere [110,111].

Carbonatites seem absent in Cambodian surface geology even though they appear in adjacent Northwestern Vietnam where rift-related carbonatites are dated at 28–44 Ma (biotite K-Ar ages) and 30–32 Ma (U-Th-Pb isochron ages) in South Nam Xe [112]. Geochemically, these carbonatites suggest involvement of an enriched mantle component in their genesis. These HSFE-deficient rocks, however, are low in Zr and lack zircon. Cenozoic carbonatite intrusions (12–40 Ma) lie 1600 km to the north within the SW China craton (Mianning-Denchang intrusive belt [113]). For the RVP magmatic sources, with a predisposition to crystallize carbonatitic-type zircon, their exact nature remains uncertain.

The absence of surficial carbonatites does not preclude a carbonatized mantle source [114]. Several types of continental carbonatitic-influenced mantle sources are known to have the potential to generate zircon megacrysts of an RVP type. Asian examples include: (1) stratified mantle deduced from ultramafic xenoliths that show initial silicate and then carbonatitic metasomatism in kamafugites from Western Qinlan, Central China [115], and (2) Pacific slab-induced carbonatitic metasomatism in garnet-bearing lherzolite xenoliths from Cenozoic basalts in NE China [116–118]. The latter is related to alkali basalts at Changle where zircon megacrysts have Hf-Y ranges similar to those in RVP zircons and the carbonatitic-modified mantle is recognized [13]. Elsewhere, upper mantle xenoliths with carbonatitic reactions are recorded in young basalt fields in SE Australia [119]. Vent deposits in this field include zircon megacrysts that show transitional silicate-carbonatitic affinities [120].

The extent to which carbonatitic altered mantle sources have contributed to zircon megacryst suites along Western Pacific continental margins remain uncertain. This uncertainty stems from the patchy spread of carbonatitic fields within the classification and regression trees CART discrimination model and the availability of inclusion and geochemical data furnished from the zircon-related host basalts [11]. A study of mantle xenoliths from young basalts on the Leizhou Peninsula, which is adjacent to the Pengali, Hainan Island mantle zircon xenocryst suites detailed a range of mantle melting and metasomatic effects [13,121]. The study identified trace element diffusion effects within the mantle and showed that HFSE depletions in metasomatized lherzolite do not necessarily require a carbonatitic metasomatizing agent.

5.4. Variation in Zircon-Bearing Xenocryst Assemblages in SE Asia

The enigmatic associations of zircon and corundum xenocrysts in intraplate alkaline basalt provinces continue to raise questions about their petrogenesis. The highly zircon-dominated RVP xenocryst suite, with minor corundum, is rare among the many basaltic gem deposits along West Pacific continental margins; corundum is common elsewhere in Cambodia (Pailin), through much of SE Asia and along Eastern Australia [8]. The lack of corundum in RVP alkali basalts suggests that particular mantle conditions favored RVP zircon genesis.

Some clues to these conditions may be offered by a study of zircon and corundum (sapphire)-bearing albititic dykes exposed within mantle assemblages in the French Pyrenees [122,123].

Some dykes contain only zircon megacrysts, some contain zircon + corundum, and some contain only corundum. Zircon in corundum-free dykes have systematically lower Hf (0.46–0.68 wt % Hf) and lower Y (740–1850 ppm), which is similar to that observed in the RVP zircon while zircon accompanied by corundum has higher values (Hf up to 1.8 wt %, Y up to 13,000 ppm). Geochemically, these dykes indicate a mantle origin, which is the result of very low degrees of partial melting (<1%) of a harzburgite source that has undergone metasomatism by a carbonatitic fluid phase prior to crystallization of the mega-crysts. To answer this dichotomy in megacryst generation, Pin et al. [123] attributed zircon formation to more CO_2-rich fluid conditions relative to more hydrous conditions for corundum formation within the feldspathic melts in the dykes during high pressure crystallization of the assemblage on the liquidus.

5.5. Models for Generation of RVP Zircon-Rich, Corundum-Poor Gem Suite

Explanations for the distinct zircon generations (low-Hf isolated zircon versus high-Hf zircon associated with corundum) along with associated megacrysts (anorthoclase) include low degrees of partial melting of the upper mantle coupled with metasomatism by a carbonatitic melt/fluid, the immiscibility of a silico-carbonatitic melt, or the interaction of carbonatitic and syenitic melts within the SCLM [86,100,124]. Both alkali basalt magmas and their mantle source regions are known sources of CO_2 and, in intraplate continental basalts, CO_2 is the main volatile [125].

At pressures ~20 kbar, CO_2 solubility increases dramatically, which promotes low-T melting of peridotite (<1000 °C) as well as significantly lowering of SiO_2 contents in resultant partial melts [114]. Very small degrees of partial melting (<1%) of a peridotite or a harzburgite at upper mantle conditions can produce early liquids strongly enriched in Si, Na, and Al and depleted in Fe, Mg, Ca, and Ti, which is similar in composition to syenite melts [122,123]. If such alkali-rich partial melt further undergoes enrichment by an H_2O-rich or CO_2-rich metasomatizing fluid, the behavior and activity of Si and Al are affected. The addition of H_2O to the metasomatizing fluid increases corundum saturation but does not affect Zr solubility [19]. The degree of partial melting, Zr content, alkalinity, and the degree of Al saturation of this silicate melt will be the determining factors in producing low-Hf or high-Hf zircon and corundum. Any carbonatitic melt fraction will reject HFSE (Zr, Hf) and preferentially incorporate LREE elements, which will result in an HFSE-HREE-enriched silicate melt. Foley et al. [114] performed partial melting experiments on peridotite with H_2O and CO_2 in which early melts are carbonate-rich and progress to carbonated silicateelts with further melting. Hafnium along with Nb and Ta show limited compatibility with early carbonate-dominant melts but are enriched in carbonated silicate melts at higher degrees of partial melting. This suggests that low-Hf zircon may crystallize in a carbonate-dominant environment while high-Hf zircon and associated Nb-Ta oxide phases are products of a carbonated silicate melt that has undergone Al-saturation. Saturation of a peralkaline melt in zircon requires orders of magnitude higher Zr content than in peraluminous melts [22,126]. Higher Zr contents in early peralkaline, carbonate-dominated melts may be responsible for the dominance of zircon over corundum in certain deposits such as in the RVP gem field.

The minor high-Hf zircon included in rare RVP corundum xenocrysts distinctly differs in morphology and geochemistry to the low-Hf mantle-derived zircon and suggests a separate, limited genesis. The high Hf-zircon resemble examples in Dak Nong, Vietnam sapphires that have crystal O isotope values and contain fluid inclusions suggestive of lower pressure crystallization from a hydrous CO_2/CO_3^{2-}-saturated melt [7,100]. As seen in the RVP zircon relationship, the Dak Nong corundum accompanies lower-Hf zircon xenocrysts, which were assigned to higher-pressure origin from melt enriched in but not saturated in CO_2.

6. Conclusions

Xenocrystic zircon from Cenozoic alkali basalts of the Ratanakiri Volcanic Province represent a unique suite within the larger zircon megacryst Indo-Pacific zone (ZIP). Crystal morphology, compositional zoning, and trace element geochemistry indicate single-stage growth within a

primary, mantle-derived alkaline melt at temperatures between 601 and 739 °C. The RVP zircon have lower δ^{18}O isotope compositions than observed in xenocrysts from other ZIP suites and a moderate range of Hf isotopic compositions, which suggest crystallization from a juvenile, alkaline lithospheric mantle magma source with limited supracrustal contamination. The xenocrysts have been dated by U-Pb (0.88–1.56 Ma) and (U-Th)/He (0.86–1.02 Ma) methods and give ages that are similar to those obtained for zircon xenocrysts from other alkali basalt provinces in SE Asia. The RVP zircon predate some of the alkali basalts (~0.7 Ma), which indicates very short mantle residence times before entrainment in the erupting magma and an earlier beginning of basaltic volcanism. The SCLM underneath the RVP is a complex region consisting of remnants of multiple rift-arc-related and back-arc-related collisional margins including the Song Ma suture zone and back margins of the Himalayan collision zone. The overriding conclusion is of crystallization from a metasomatized "carbonatitic"-influenced melt from very low partial melting of a peridotite SCLM source at about 60 km beneath the Indochina terrain.

References

1. Shor, R.; Weldon, R. Ruby and sapphire production and distribution: A quarter century of change. *Gems Gemol.* **2009**, *45*, 236–259. [CrossRef]
2. Smith, M.H.; Balmer, W.A. Zircon Mining in Cambodia. *Gems Gemol.* **2009**, *45*, 152–154.
3. Schwarz, D. Coloured gemstones—Mines and Markets. In Proceedings of the 34th International Gemmological Conference, Vilnius, Lithuania, 25–30 August 2015; pp. 110–112.
4. Abduriyim, A.; Sutherland, F.L.; Belousova, E.A. U-Pb age and origin of gem zircon from the New England sapphire fields, New South Wales, Australia. *Aust. J. Earth Sci.* **2012**, *59*, 1067–1081. [CrossRef]
5. Belousova, E.A.; Griffin, W.L.; O'Reilly, S.Y.; Fisher, N. Igneous zircon: Trace element composition as an indicator of source rock type. *Contrib. Mineralog. Petrol.* **2002**, *143*, 602–622. [CrossRef]
6. Chen, T.; Ai, H.; Yang, M.; Zheng, S.; Liu, Y. Brownish Red Zircon from Muling, China. *Gems Gemol.* **2011**, *47*, 36–41. [CrossRef]
7. Garnier, V.; Ohnenstetter, D.; Guliani, G.; Fallick, A.E.; Trong, T.P.; Quang, V.H.; Van, L.P.; Schwarz, D. Basalt petrology, zircon ages and sapphire genesis from Dak Nong, southern Vietnam. *Mineral. Mag.* **2005**, *69*, 21–38. [CrossRef]

8. Graham, I.; Sutherland, L.; Zaw, K.; Nechaev, V.; Khanchuk, A. Advances in our understanding of the gem corundum deposits of the West Pacific continental margins intraplate basaltic fields. *Ore Geol. Rev.* **2008**, *34*, 200–215. [CrossRef]

9. Qiu, Z.; Wu, F.; Yu, Q.; Xie, L.; Yang, S. Hf isotopes of zircon megacrysts from the Cenozoic basalts in eastern China. *Chin. Sci. Bull.* **2005**, *50*, 2602–2611. [CrossRef]

10. Sutherland, F.L.; Coenraads, R.R.; Abduriyim, A.; Meffre, S.; Hoskin, P.W.O.; Giuliani, G.; Beattie, R.; Wuhrer, R.; Sutherland, G.B. Corundum (sapphire) and zircon relationships, Lava Plains gem fields, NE Australia: Integrated mineralogy, geochemistry, age determination, genesis and geographical typing. *Mineral. Mag.* **2015**, *79*, 545–581. [CrossRef]

11. Sutherland, F.L.; Graham, I.; Yaxley, G.; Armstrong, R.; Giuliani, G.; Hoskin, P.; Nechaev, V.; Woodhead, J. Major zircon megacryst suites of the Indo-Pacific lithospheric mrgin (ZIP) and their petrogenetic and regional implications. *Mineral. Petrol.* **2016**, *110*, 399–420. [CrossRef]

12. Sutherland, F.L.; Piilonen, P.C.; Zaw, K.; Meffre, S.; Thompson, J. Sapphire within zircon-rich gem deposits, Bo Loei, Ratanakiri Province, Cambodia: Trace elements, inclusions, U-Pb dating and genesis. *Aust. J. Earth Sci.* **2015**, *62*, 761–773. [CrossRef]

13. Yu, Y.; Xu, X.; Chen, X. Genesis of zircon megacrysts in Cenozoic alkali basalts and the heterogeneity of subcontinental lithospheric mntle, eastern China. *Mineral. Petrol.* **2010**, *100*, 75–94. [CrossRef]

14. Zaw, K.; Sutherland, F.L.; Dellapasqua, F.; Ryan, C.G.; Yui, T.-F.; Mernagh, T.P.; Duncan, D. Contrasts in gem corundum characteristics, eastern Australian basaltic fields: Trace elements, fluid/melt inclusions and oxygen isotopes. *Mineral. Mag.* **2006**, *70*, 669–687. [CrossRef]

15. Fan, P.-F. Tectonic patterns and Cenozoic basalts in the western mrgin of the South China Sea. *Geol. Soc. Malays. Bull.* **1995**, *37*, 91–97.

16. Fedorov, P.I.; Koloskov, A.V. Cenozoic volcanism of southeast Asia. *Petrology* **2005**, *13*, 352–380.

17. Taylor, J.G.C.; Buravas, S. Gem deposits at Khao Ploi Waen and Bang Ka Cha, Chanthaburi Province. In *Geologic Reconnaissance of the mineral Deposits of Thailand*; United States Government Printing Office: Washington, WA, USA, 1951; Volume 984, pp. 144–148.

18. Harley, S.L.; Kelly, N.M. Zircon Tiny but Timely. *Elements* **2007**, *3*, 13–18. [CrossRef]

19. Boehnke, P.; Watson, E.B.; Trail, D.; Harrison, T.M.; Schmitt, A.K. Zircon saturation re-revisited. *Chem. Geol.* **2013**, *351*, 324–334. [CrossRef]

20. Watson, E.B. Zircon saturation in felsic liquids: Experimental results and applications to trace element geochemistry. *Contrib. Mineral. Petrol.* **1979**, *70*, 407–419. [CrossRef]

21. Watson, E.B.; Harrison, T.M. Zircon saturation revisited: Temperature and composition effects in a variety of crustal mgma types. *Earth Planet. Sci. Lett.* **1983**, *64*, 295–304. [CrossRef]

22. Linnen, R.L.; Keppler, H. Melt composition control of Zr/Hf fractionation in mgmatic processes. *Geochim. Cosmochimi. Acta* **2002**, *66*, 3293–3301. [CrossRef]

23. Cong, F.; Li, S.-Q.; Lin, F.-C.; Shi, M.-F.; Zhu, H.-P.; Siebel, W.; Chen, F. Origin of Zircon Megacrysts from Cenozoic Basalts in Northeastern Cambodia: Evidence from U-Pb Age, Hf-O Isotopes, and Inclusions. *J. Geol.* **2016**, *124*, 221–234. [CrossRef]

24. Ridd, M.F.; Barber, A.J.; Crow, M.J. Introduction to the geology of Thailand. In *Geology of Thailand*; Ridd, M.F., Barber, A.J., Crow, M.J., Eds.; The Geological Society: London, UK, 2011; pp. 1–17.

25. Searle, M.P.; Morley, C.K. Tectonic and thermal evolution of Thailand in the regional context of SE Asia. In *Geology of Thailand*; Ridd, M.F., Barber, A.J., Crow, M.J., Eds.; The Geological Society: London, UK, 2011; pp. 539–571.

26. Workman, D.R. Geology of Laos, Cambodia, South Vietnam and the eastern part of Thailand. *Overseas Geol. Miner. Resour.* **1977**, *50*, 1–34.

27. Sotham, S. Geology of Cambodia. *CCOP Tech. Bull.* **1997**, *26*, 13–23.

28. Khain, V.E. *Tectonics of the Continents and Oceans*; Nauchny Mir: Moscow, Russia, 2001.

29. Mukasa, S.B.; matthew Fischer, G.; Barr, S.M. The Character of the Subcontinental Mantle in Southeast Asia: Evidence From Isotopic and Elemental Compositions of Extension-Related Cenozoic Basalts in Thailand. In *Earth Processes: Reading the Isotopic Code*; Basu, A., Hart, S., Eds.; Geophysical Monograph-American Geophysical Union: Washington DC, WA, USA, 1996; Volume 95, pp. 233–252.

30. Le Pichon, X.; Fournier, M.; Jolivet, L. Kinematics, topography, shortening, and extrusion in the India-Eurasia collision. *Tectonics* **1992**, *11*, 1085–1098. [CrossRef]

31. Miller, M.S.; Kennett, B.L.N.; Toy, V.G. Spatial and temporal evolution of the subducting Pacific plate structure along the western Pacific margin. *J. Geophys. Res.* **2006**, *111*, B02401. [CrossRef]

32. Sutherland, F.L. Alkaline rocks and gemstones, Australia: A review and synthesis. *Aust. J. Earth Sci.* **1996**, *43*, 323–343. [CrossRef]

33. Sutherland, F.L.; Fanning, C.M. Gem-bearing basaltic volcanism, Barrington, New South Wales: Cenozoic evolution, based on basalt K-Ar ages and zircon fission track and U-Pb isotope dating. *Aust. J. Earth Sci.* **2001**, *48*, 221–237. [CrossRef]

34. Patte, E. Etude de l'ile des Cendres, volcan apparu au large de la côte d'Annam. *Bull. Serv. Géol. l'Indoch.* **1925**, *13*, 1–19.

35. Saurin, E. La néotectonique de l'Indochine. *Rev. Géogr. Phys. Géol. Dyn.* **1967**, *9*, 143–151.

36. Barr, S.M.; MacDonald, A.S. Geochemistry and petrogenesis of Late Cenozoic alkaline basalts of Thailand. *Geol. Soc. Malays. Bull.* **1978**, *10*, 25–52.

37. Barr, S.M.M.; Alan, S. Geochemistry and Geochronology of Late Cenozoic Basalts of Southeast Asia. *GSA Bull.* **1981**, *92*, 1069–1142. [CrossRef]

38. Sutherland, F.L.; Bosshart, G.; Fanning, C.M.; Hoskin, P.W.O.; Coenraads, R.R. Sapphire crystallization, age and origin, Ban Huai Sai, Laos: Age based on zircon inclusions. *J. Asian Earth Sci.* **2002**, *20*, 841–849. [CrossRef]

39. Barr, S.M.J.; Dodie, E. Trace element characteristics of Upper Cenozoic basaltic rocks of Thailand, Kampuchea and Vietnam. *J. Southeast Asian Earth Sci.* **1990**, *4*, 233–242. [CrossRef]

40. Hoang, N.; Flower, M. Petrogenesis of Cenozoic Basalts from Vietnam: Implication for Origins of a 'Diffuse Igneous Province'. *J. Petrol.* **1998**, *39*, 369–395. [CrossRef]

41. Barr, S.M.; Charusiri, P. Volcanic rocks. In *The Geology of Thailand*; Ridd, M.F., Barber, A.J., Crow, M.J., Eds.; The Geological Society: London, UK, 2011; pp. 415–438.

42. Lacombe, P. La mssif basaltique quaternaire à zircons-gemmes de Ratanakiri (Cambodge nord-oriental)—Premiére partie. *Bull. Rech. Géol. min.* **1969**, *3*, 31–91.

43. Lacombe, P. La mssif basaltique quaternaire à zircons-gemmes de Ratanakiri (Cambodge nord-oriental)-Troisiéme partie: Minéralogie et géologie des gisements de zircons. *Bull. Rech. Géol. Min.* **1970**, *4*, 33–79.

44. Whitford-Stark, J.L. A survey of Cenozoic volcanism on mainland Asia. In *Geological Society of America Special Paper*; Geological Society of America: Boulder, CO, USA, 1987; Volume 213.

45. Zeug, M.; Nasdala, L.; Wanthanachaisaeng, B.; Balmer, W.A.; Corfu, F.; Wildner, M. Blue Zircon from Ratanakiri, Cambodia. *J. Gemmol.* **2018**, *36*, 112–132. [CrossRef]

46. Pouchou, J.L.; Pichoir, F. *'PAP'j(rZ) Procedure for Improved Quantitative Microanalysis*; San Francisco Press: San Francisco, CA, USA, 1984.

47. Elhlou, S.; Belousova, E.A.; Griffin, W.L.; Pearson, N.J.; O'Reilly, S.Y. Trace element and isotopic composition of GJ-red zircon standard by laser ablation. *Geochim. Cosmochim. Acta* **2006**, *70*, A158. [CrossRef]

48. Griffin, W.L.; Pearson, N.J.; Belousova, E.; Jackson, S.E.; van Achterbergh, E.; O'Reilly, S.Y.; Shee, S.R. The Hf isotope composition of cratonic mntle: LAM-MC-ICPMS analysis of zircon megacrysts in kimberlites. *Geochim. Cosmochi. Acta* **2000**, *64*, 133–147. [CrossRef]

49. DeBievre, P.; Taylor, P.D.P. Table of the isotopic composition of the elements. *Int. J. Mass Spectrom. Ion Process.* **1993**, *123*, 149–166. [CrossRef]

50. Pearson, N.J.; Griffin, W.L.; O'Reilly, S.Y. Mass fractionation correction in laser ablation-multiple collector ICP-MS: Implications for overlap corrections and precise and accurate in situ isotope ratio measurement. In *Laser-Ablation ICP-MS in the Earth Sciences*; Sylvester, P.J., Ed.; mineralogical Association of Canada: Quebec City, QC, Canada, 2008; Volume 40, pp. 93–116.

51. Griffin, W.L.; Pearson, N.J.; Belousova, E.A.; Saeed, A. Reply to "Comment to short-communication 'Comment: Hf-isotope heterogeneity in zircon 91500' by W.L. Griffin, N.J. Pearson, E.A. Belousova and A. Saeed [Chemical Geology 233 (2006) 358-363]" by F. Corfu. *Chem. Geol.* **2007**, *244*, 354–356. [CrossRef]

52. Kemp, A.I.S.; Wormald, R.J.; Whitehouse, M.J.; Price, R.C. Hf isotopes in zircon reveal contrasting sources and crystallization histories for alkaline to peralkaline granites of Temora, southeastern Australia. *Geology* **2005**, *33*, 797–800. [CrossRef]

53. Bouvier, A.; Vervoort, J.D.; Patchett, P.J. The Lu-Hf and Sm-Nd isotopic composition of CHUR: Constraints from unequilibrated chondrites and implications for the bulk composition of terrestrial planets. *Earth Planet. Sci. Lett.* **2008**, *273*, 48–57. [CrossRef]

54. Scherer, E.; Münker, C.; Mezger, K. Calibration of the Lutetium-Hafnium Clock. *Science* **2001**, *293*, 683–687. [CrossRef] [PubMed]

55. Jackson, S.E.; Pearson, N.J.; Griffin, W.L.; Belousova, E.A. The application of laser ablation microprobe-inductively coupled plasma-mass spectrometry (LAM-ICPMS) to in situ U-Pb zircon geochronology. *Chem. Geol.* **2004**, *211*, 47–69. [CrossRef]

56. Griffin, W.L.; Powell, W.J.; Pearson, N.J.; O'Reilly, S.Y. GLITTER: Data reduction software for laser ablation ICP-MS. In *Laser Ablation ICP-MS in the Earth Sciences*; Sylvester, P.J., Ed.; Mineralogical Association of Canada: Quebec City, QC, Canada, 2008; pp. 204–207.

57. Andersen, T. Correction of common lead in U-Pb analyses that do not report 204Pb. *Chem. Geol.* **2002**, *192*, 59–79. [CrossRef]

58. Stacey, J.S.T.; Kramers, J.D. Approximation of terrestrial lead isotope evolution by a two-stage model. *Earth Planet. Sci. Lett.* **1975**, *26*, 207–221. [CrossRef]

59. Reiners, P.W.; Spell, T.L.; Nicolescu, S.; Zanetti, K.A. Zircon (U-Th)/He thermochronometry: He diffusion and comparisons with ^{40}Ar/^{39}Ar dating. *Geochim Cosmochim. Acta* **2004**, *68*, 1857–1887. [CrossRef]

60. Danišík, M.; Kuhlemann, J.; Dunkl, I.; Evans, N.J.; Székely, B.; Frisch, W. Survival of Ancient Landforms in a Collisional Setting as Revealed by Combined Fission Track and (U-Th)/He Thermochronometry: A Case Study from Corsica (France). *J. Geol.* **2012**, *120*, 155–173. [CrossRef]

61. Danišík, M.; Štěpančíková, P.; Evans, N.J. Constraining long-term denudation and faulting history in intraplate regions by multisystem thermochronology: An example of the Sudetic Marginal Fault (Bohemian Massif, central Europe). *Tectonics* **2012**, *31*. [CrossRef]

62. Farley, K.A.; Wolf, R.A.; Silver, L.T. The effects of long alpha-stopping distances on (U-Th)/He ages. *Geochim. Cosmochim. Acta* **1996**, *60*, 4223–4229. [CrossRef]

63. Vermeesch, P. HelioPlot, and the treatment of overdispersed (U-Th-Sm)/He data. *Chem. Geol.* **2010**, *271*, 108–111. [CrossRef]

64. Reiners, P.W. Zircon (U-Th)/He Thermochronometry. *Rev. Mineral. Geochem.* **2005**, *58*, 151–179. [CrossRef]

65. Valley, J.W.; Chiarenzelli, J.R.; McLelland, J.M. Oxygen isotope geochemistry of zircon. *Earth Planet. Sci. Lett.* **1994**, *126*, 187–206. [CrossRef]

66. Valley, J.W.; Kitchen, N.; Kohn, M.J.; Niendorf, C.R.; Spicuzza, M.J. UWG-2, a garnet standard for oxygen isotope ratios: Strategies for high precision and accuracy with laser heating. *Geochim. Cosmochim. Acta* **1995**, *59*, 5223–5231. [CrossRef]

67. Pupin, J.-P. Zircon and granite petrology. *Contrib. Mineral. Petrol.* **1980**, *73*, 207–220. [CrossRef]

68. Shore, M.; Fowler, A.D. Oscillatory zoning in minerals: A common phenomenon. *Can. Mineral.* **1996**, *34*, 1111–1126.

69. Witter, A.; Nasdala, L.; Wanthanachaisaeng, B.; Bunnag, N.; Škoda, R.; Balmer, W.A.; Geister, G.; Zeug, M. Mineralogical characterization of gem zircon from Ratanakiri, Cambodia. In Proceedings of the CORALS 2013, Vienna, Austria, 3–6 July 2013.

70. McDonough, W.F.; Sun, S.S. The composition of the Earth. *Chem. Geol.* **1995**, *120*, 223–253. [CrossRef]

71. Pupin, J.P. *Transactions of the Royal Society of Edinburgh, Earth Sciences*; RSE Scotland Foundation: Edinburgh, UK, 2000.

72. Watson, E.B.; Harrison, T.M. Zircon Thermometer Reveals minimum Melting Conditions on Earliest Earth. *Science* **2005**, *308*, 841–844. [CrossRef] [PubMed]

73. Watson, E.B.; Wark, D.A.; Thomas, J.B. Crystallization thermometers for zircon and rutile. *Contrib. Mineral. Petrol.* **2006**, *151*, 413–433. [CrossRef]

74. Fu, B.; Page, F.Z.; Cavosie, A.J.; Fournelle, J.; Kita, N.T.; Lackey, J.S.; Wilde, S.A.; Valley, J.W. Ti-in-zircon thermometry: Applications and limitations. *Contrib. Mineral. Petrol.* **2008**, *156*, 197–215. [CrossRef]

75. Cherniak, D.J.; Watson, E.B. Ti diffusion in zircon. *Chem. Geol.* **2007**, *242*, 470–483. [CrossRef]

76. Crisp, L. The effect of pressure on Ti-in-zircon and Zr-in-rutile. In Proceedings of the Petrology and geochemistry seminars, Research School of Earth Sciences, Canberra, Australia, 29 May 2015.

77. Page, F.Z.; Fu, B.; Kita, N.T.; Fournelle, J.; Spicuzza, M.J.; Schulze, D.J.; Viljoen, F.; Basei, M.A.S.; Valley, J.W. Zircons from kimberlite: New insights from oxygen isotopes, trace elements, and Ti in zircon thermometry. *Geochim. Cosmochim. Acta* **2007**, *71*, 3887–3903. [CrossRef]

78. Carbonnel, J.-P.; Duplaix, S.; Selo, M. La méthode des traces de fission de l'U apliquée á la géochronologic. Datation du magmatisme récente de I'Asie du Sud-Est. *Rev. Géogr. Phys. Geolo. Dyn.* **1972**, *14*, 29–46.

79. Carbonnel, J.-P.; Selo, M.; Poupeau, G. Fission track age of the gem deposit of Pailin (Cambodia) and recent tectonics in the Indochinan province. *Mod. Geol.* **1973**, *4*, 61–64.

80. Li, X.-H.; Long, W.-G.; Li, Q.-L.; Liu, Y.; Zheng, Y.-F.; Yang, Y.-H.; Chamberlain, K.R.; Wan, D.-F.; Guo, C.-H.; Wang, X.-C.; et al. Penglai Zircon Megacrysts: A Potential New Working Reference Material for Microbeam Determination of Hf-O Isotopes and U-Pb Age. *Geostand. Geoanal. Res.* **2010**, *34*, 117–134. [CrossRef]

81. Li, Y.; Zheng, D.; Wu, Y.; Wang, Y.; He, H.; Pang, J.; Wang, Y.; Yu, J. A Potential (U-Th)/He Zircon Reference Material from Penglai Zircon Megacrysts. *Geostand. Geoanal. Res.* **2017**, *41*, 359–365. [CrossRef]

82. Dodson, M.H. Closure temperature in cooling geochronological and petrological systems. *Contrib. Mineral. Petrol.* **1973**, *40*, 259–274. [CrossRef]

83. Page, F.Z.; Ushikubo, T.; Kita, N.T.; Riciputi, L.R.; Valley, J.W. High-precision oxygen isotope analysis of picogram samples reveals 2 μm gradients and slow diffusion in zircon. *Am. Mineral.* **2007**, *92*, 1772–1775. [CrossRef]

84. Bowman, J.R.; Moser, D.E.; Valley, J.W.; Wooden, J.L.; Kita, N.T.; Mazdab, F.K. Zircon U-Pb isotope, δ^{18}O and trace element response to 8o m.y. of high temperature metamorphism in the lower crust: Sluggish diffusion and new records of Archean craton formation. *Am. J. Sci.* **2011**, *311*, 719–772. [CrossRef]

85. Mattey, D.; Lowry, D.; Macpherson, C. Oxygen isotope composition of mntle peridotite. *Earth Planet. Sci. Lett.* **1994**, *128*, 231–241. [CrossRef]

86. Upton, B.G.J.; Hinton, R.W.; Aspen, P.; Finch, A.; Valley, J.W. Megacrysts and Associated Xenoliths: Evidence for Migration of Geochemically Enriched Melts in the Upper Mantle beneath Scotland. *J. Petrol.* **1999**, *40*, 935–956. [CrossRef]

87. Valley, J.W.; Kitchen, N.; Kohn, M.J.; Niendorf, C.R.; Spicuzza, M.J. Oxygen Isotopes in Zircon. In *Reviews in Mineralogy and Geochemistry*; Hanchar, J.M., Hoskin, P.W.O., Eds.; Mineralogical Society of America: Chantilly, VA, USA, 2003; Volume 53, pp. 343–385.

88. Belousova, E.A.; Griffin, W.L.; O'Reilly, S.Y. Zircon Crystal Morphology, Trace Element Signatures and Hf Isotope Composition as a Tool for Petrogenetic Modelling: Examples From Eastern Australian Granitoids. *J. Petrol.* **2006**, *47*, 329–353. [CrossRef]

89. Heaman, L.M.; Bowins, R.; Crocket, J. The chemical composition of igneous zircon suites: Implications for geochemical tracer studies. *Geochim. Cosmochim. Acta* **1990**, *54*, 1597–1607. [CrossRef]

90. Hoskin, P.W.O.; Ireland, T.R. Rare earth element chemistry of zircon and its use as a provenance indicator. *Geology* **2000**, *28*, 627–630. [CrossRef]

91. Seifert, W.; Rhede, D.; Tietz, O. Typology, chemistry and origin of zircon from alkali basalts of SE Saxony (Germany). *N. Jahrb. Mineralo. Abh.* **2008**, *184*, 299–313. [CrossRef]

92. Shnukov, S.E.; Andreev, A.V.; Savenok, S.P. Admixture elements in zircons and apatites: A tool for provenance studies of terrigenous sedimentary rocks. In Proceedings of the European Union of Geosciences (EUG 9), Strasbourg, France, 23–27 March 1997.

93. Pupin, J.-P. Granite genesis related to geodynamics from Hf-Y in zircon. *Earth Environ. Sci. Trans. R. Soc. Edinb.* **2000**, *91*, 245–256. [CrossRef]

94. Visonà, D.; Caironi, V.; Carraro, A.; Dallai, L.; Fioretti, A.M.; Fanning, M. Zircon megacrysts from basalts of the Venetian Volcanic Province (NE Italy): U-Pb ages, oxygen isotopes and REE data. *Lithos* **2007**, *94*, 168–180. [CrossRef]

95. Hoskin, P.W.O.; Schaltegger, U. The Composition of Zircon and Igneous and Metamorphic Petrogenesis. *Rev. Mineral. Geochem.* **2003**, *53*, 27–62. [CrossRef]

96. Borghini, G.; Fumagalli, P.; Rampone, E. The Stability of Plagioclase in the Upper Mantle: Subsolidus Experiments on Fertile and Depleted Lherzolite. *J. Petrol.* **2010**, *51*, 229–254. [CrossRef]

97. Hinton, R.W.; Upton, B.G.J. The chemistry of zircon: Variations within and between large crystals from syenite and alkali basalt xenoliths. *Geochim. Cosmochim. Acta* **1991**, *55*, 3287–3302. [CrossRef]

98. Coenraads, R.R.; Vichit, P.; Sutherland, F.L. An unusual sapphire-zircon-magnetite xenolith from the Chanthaburi Gem Province, Thailand. *Mineral. Mag.* **1995**, *59*, 465–479. [CrossRef]

99. Khamloet, P.; Pisutha-Arnond, V.; Sutthirat, C. Mineral inclusions in sapphire from the basalt-related deposit in Bo Phloi, Kanchanaburi, western Thailand: Indication of their genesis. *Russ. Geol. Geophys.* **2014**, *55*, 1087–1102. [CrossRef]

100. Izokh, A.E.; Smirnov, S.Z.; Egorova, V.V.; Tuan Anh, T.; Kovyazin, S.V.; Phuong, N.T.; Kalinina, V.V. The conditions of formation of sapphire and zircon in the areas of alkali-basaltoid volcanism in Central Vietnam. *Russ. Geol. Geophys.* **2010**, *51*, 719–733. [CrossRef]

101. Guo, J.; O'Reilly, S.Y.; Griffin, W.L. Corundum from basaltic terrains: A mineral inclusion approach to the enigma. *Contrib. Mineral. Petrol.* **1996**, *122*, 368–386. [CrossRef]

102. Guo, J.; O'Reilly, S.Y.; Griffin, W.L. Zircon inclusions in corundum megacrysts: I. Trace element geochemistry and clues to the origin of corundum megacrysts in alkali basalts. *Geochim. Cosmochim. Acta* **1996**, *60*, 2347–2363. [CrossRef]

103. Sutherland, F.L.; Hoskin, P.W.O.; Fanning, C.M.; Coenraads, R.R. Models of corundum origin from alkali basaltic terrains: A reappraisal. *Contrib. Mineral. Petrol.* **1998**, *133*, 356–372. [CrossRef]

104. Benisek, A.; Finger, F. Factors controlling the development of prism faces in granite zircons: A microprobe study. *Contrib. Mineral. Petrol.* **1993**, *114*, 441–451. [CrossRef]

105. Grimes, C.B.; John, B.E.; Kelemen, P.B.; Mazdab, F.K.; Wooden, J.L.; Cheadle, M.J.; Hanghøj, K.; Schwartz, J.J. Trace element chemistry of zircons from oceanic crust: A method for distinguishing detrital zircon provenance. *Geology* **2007**, *35*, 643–646. [CrossRef]

106. Grimes, C.B.; Wooden, J.L.; Cheadle, M.J.; John, B.E. "Fingerprinting" tectono-magmatic provenance using trace elements in igneous zircon. *Contrib. Mineral. Petrol.* **2015**, *170*, 92–117. [CrossRef]

107. Liu, Y.; Williams, I.S.; Chen, J.; Wan, Y.; Sun, W. The significance of Paleoproterozoic zircon in carbonatite dikes associated with the Bayan Obo REE-Nb-Fe deposit. *Am. J. Sci.* **2008**, *308*, 379–397. [CrossRef]

108. Campbell, L.S.; Compston, W.; Sircombe, K.N.; Wilkinson, C.C. Zircon from the East Orebody of the Bayan Obo Fe-Nb-REE deposit, China, and SHRIMP ages for carbonatite-related mgmatism and REE mineralization events. *Contrib. Mineral. Petrol.* **2014**, *168*, 1041. [CrossRef]

109. Saava, E.V.; Belyatsky, B.V.; Antonov, A.B. Carbonatitic Zircon-Myth or Reality: Mineralogical-Geochemical Analyses. Available online: http://alkaline09.narod.ru/abstracts/Savva_Belyatsky.htm (accessed on 26 October 2018).

110. Bell, K.; Simonetti, A. Source of parental melts to carbonatites—Critical isotopic constraints. *Mineral. Petrol.* **2010**, *98*, 77–89. [CrossRef]

111. Chakmouradian, A. The geochemistry of continental carbonatites revisited: Two mjor types of continental carbonatites and their trace-element signatures. In Proceedings of the European Geosciences Union General Assembly, Vienna, Austria, 19–24 April 2009; p. 10806.

112. Thi, T.N.; Wada, H.; Ishikawa, T.; Shimano, T. Geochemistry and petrogenesis of carbonatites from South Nam Xe, Lai Chau area, northwest Vietnam. *Mineral. Petrol.* **2014**, *108*, 371–390.

113. Hou, Z.; Liu, Y.; Tian, S.; Yang, Z.; Xie, Y. Formation of carbonatite-related giant rare-earth-element deposits by the recycling of mrine sediments. *Sci. Rep.* **2015**, *5*, 1–10. [CrossRef] [PubMed]

114. Foley, S.F.; Yaxley, G.M.; Rosenthal, A.; Buhre, S.; Kiseeva, E.S.; Rapp, R.P.; Jacob, D.E. The composition of near-solidus melts of peridotite in the presence of CO_2 and H_2O between 40 and 60 kbar. *Lithos* **2009**, *112*, 274–283. [CrossRef]

115. Su, B.-X.; Zhang, H.-F.; Sakyi, P.A.; Ying, J.-F.; Tang, Y.-J.; Yang, Y.-H.; Qin, K.-Z.; Xiao, Y.; Zhao, X.-M. Compositionally stratified lithosphere and carbonatite metasomatism recorded in mntle xenoliths from the Western Qinling (Central China). *Lithos* **2010**, *116*, 111–128. [CrossRef]

116. Deng, L.L.; Liu, Y.; Gao, S. Pacific slab-induced carbonatite mntle metasomatism in the eastern North China Craton. In Proceedings of the American Geophysical Union Fall Meeting, San Francisco, CA, USA, 15–19 December 2014.

117. Zeng, G.; Chen, L.-H.; Xu, X.-S.; Jiang, S.-Y.; Hofmann, A.W. Carbonated mntle sources for Cenozoic intra-plate alkaline basalts in Shandong, North China. *Chem. Geol.* **2010**, *273*, 35–45. [CrossRef]

118. Deng, L.; Liu, Y.; Zong, K.; Zhu, L.; Xu, R.; Hu, Z.; Gao, S. Trace element and Sr isotope records of multi-episode carbonatite metasomatism on the eastern mrgin of the North China Craton. *Geochem. Geophys. Geosyst.* **2017**, *18*, 220–237. [CrossRef]

119. Yaxley, G.M.; Green, D.H.; Kamenetsky, V. Carbonatite Metasomatism in the Southeastern Australian Lithosphere. *J. Petrol.* **1998**, *39*, 1917–1930. [CrossRef]

120. Sutherland, F.L.; Graham, I.T.; Hollis, J.D.; Meffre, S.; Zwingmann, H.; Jourdan, F.; Pogson, R.E. Multiple felsic events within post-10 Ma volcanism, Southeast Australia: Inputs in appraising proposed magmatic models. *Aust. J. Earth Sci.* **2014**, *61*, 241–267. [CrossRef]

121. Yu, J.-H.; O'Reilly, S.Y.; Zhang, M.; Griffin, W.L.; Xu, X. Roles of Melting and Metasomatism in the Formation of the Lithospheric Mantle beneath the Leizhou Peninsula, South China. *J. Petrol.* **2006**, *47*, 355–383. [CrossRef]

122. Monchoux, P.; Fontan, F.; De Parseval, P.; Martin, R.F.; Wang, C.R. Igneous albitite dikes in orogenic lherzolites, western Pyréneés, France: A possible source for corundum and alkali feldspar xenocrysts in basaltic terraines. I. mineralogical associations. *Can. Mineral.* **2006**, *44*, 817–842. [CrossRef]

123. Pin, C.; Monchoux, P.; Paquette, J.L.; Azambre, B.; Wang, C.R.; Martin, R.F. Igneous albititic dikes in orogenic lherzolites, western Pyréneés, France: A possible source for corundum and alkali feldspar xenocrysts in basaltic terraines. II. Geochemical and petrogenetic considerations. *Can. Mineral.* **2006**, *44*, 843–856. [CrossRef]

124. Long, A.M.; Menzies, M.A.; Thirlwall, M.F.; Upton, B.G.J.; Aspen, P. Carbonatite-mantle interaction: A possible origin for megacryst/xenolith suites in Scotland. In Proceedings of the 5th International Kimberlite Conference, Araxá, Brazil, 18 June–4 July 1991; pp. 467–477.

125. Bakumenko, I.T.; Tomilenko, A.A.; Bazarova, T.Y.; Yarmolyuk, V.V. The conditions of formation of volcanics in the Late Mesozoic–Cenozoic West Trans-Baikalian volcanic area (from results of study of melt and fluid inclusions in minerals). *Geokhimiya* **1999**, *12*, 1352–1356.

126. Gervasoni, F.; Klemme, S.; Rocha-Júnior, E.R.V.; Berndt, J. Zircon saturation in silicate melts: A new and improved model for aluminous and alkaline melts. *Contrib. Mineral. Petrol.* **2016**, *171*, 21. [CrossRef]